Materials Today Energy 60 (2026) 102359

Contents lists available at ScienceDirect

Materials Today Energy

journal homepage: www.journals.elsevier.com/materials-today-energy/

2T perovskite tandem solar cells in space: Failure mechanisms and design strategies

Harini Srikanth Rao [a], Wei-Hao Chiu [b], Shih-Hsuan Chen [a], Ming-Chung Wu [a,b,c,d], Kun-Mu Lee [a,b,c,e,*]

[a] Department of Chemical and Materials Engineering, Chang Gung University, Taoyuan, 33302, Taiwan
[b] Center for Sustainability and Energy Technologies, Chang Gung University, Taoyuan, 33302, Taiwan
[c] College of Environment and Resources, Ming Chi University of Technology, New Taipei City, 24301, Taiwan
[d] Department of Materials Engineering, Ming Chi University of Technology, New Taipei, 243303, Taiwan
[e] Division of Neonatology, Department of Pediatrics, Chang Gung Memorial Hospital, Linkou, Taoyuan, 33305, Taiwan

ARTICLE INFO

Keywords:
Perovskite tandems
Space photovoltaics
Interconnecting layer
Atomic oxygen
Reliability
Encapsulation

ABSTRACT

Perovskite tandem solar cells (TSCs) offer a promising route toward lightweight, high-efficiency space photovoltaics, but their multilayer architecture introduces degradation pathways beyond those of single-junction devices. This review examines the reliability of two-terminal (2T) perovskite TSCs under space-relevant stressors, including radiation, vacuum, atomic oxygen, ultraviolet exposure, thermal cycling, and low-intensity, low-temperature operation. The discussion is organized from stressor-specific degradation to layer-wise vulnerability, covering absorber instability, charge transport layer degradation, interconnecting layer (ICL) failure, bottom-cell damage, electrode diffusion, and encapsulation limitations. Since complete tandem studies remain limited, degradation trends are interpreted using tandem sub-cell data, single-junction analogues, and material-level studies. The review also highlights how current matching and buried ICL stability can convert localized degradation into full-device performance loss. Multiscale simulation methods are discussed as tools for linking radiation, thermal, and mechanical stress to device-level outcomes. Finally, design strategies for improving stability are summarized, including absorber composition tuning, interface passivation, robust ICLs, protective barriers, and mechanically compatible encapsulation. This review provides a reliability-focused framework for developing 2T perovskite TSCs for future space missions.

1. Introduction

Space-based solar power has become the primary energy source of modern aerospace missions, providing energy for satellites, space stations, and deep-space probes since the very dawn of the space age [1]. Unlike terrestrial photovoltaics, which benefit from easy maintenance and mild conditions, space photovoltaics must operate reliably in the unforgiving vacuum of orbit and beyond. Today's increasing demand for solar power in orbit, from the swarm of small satellites in low Earth orbit (LEO) to high-power geostationary Earth orbit (GEO) communications platforms, as well as planned lunar bases and Mars expeditions, is driving a renewed focus on advanced photovoltaic technologies tailored for space [2,3]. Numerous upcoming missions (e.g. lunar Gateway stations, planetary rovers, deep-space telescopes) are being designed for harsh extraterrestrial environments, making reliable, efficient, and lightweight power systems more critical than ever. In parallel, the rise of large LEO constellations and cost-sensitive CubeSat missions has created an appetite for high-volume, low-cost solar arrays that still meet demanding performance requirements such as long end-of-life power output and high areal power density (W/m^2) [4–7].

Space missions span a range of environments, Earth orbits, lunar surface, Mars, and deep space, each imposing distinct stressors on solar cells. In LEO, satellites endure an extreme ultraviolet (UV) flux and atomic oxygen (AO) bombardment while repeatedly cycling in and out of sunlight every ~90 min. This causes drastic temperature swings (e.g. the International Space Station (ISS) ranges from >100 °C in sun to below −100 °C in shadow) and material erosion from reactive oxygen. By contrast, GEO offers constant solar illumination but ultra-high vacuum and a harsher radiation environment, including high-energy electron radiation and trapped particle radiation. The absence of AO in GEO

* Corresponding author. Department of Chemical and Materials Engineering, Chang Gung University, Taoyuan, 33302, Taiwan.
E-mail address: KMLee@mail.cgu.edu.tw (K.-M. Lee).

https://doi.org/10.1016/j.mtener.2026.102359
Received 27 May 2026; Received in revised form 28 June 2026; Accepted 12 July 2026
Available online 13 July 2026

eliminates oxygen erosion, though outgassing of volatile materials under deep vacuum can be a concern. On the Moon, photovoltaic (PV) systems must survive 14-day light/dark cycles, surface temperature reaches ~123 °C at noon and plummets to ~ -178 °C at night. Lunar panels also face micrometeoroid impacts, abrasive dust, and unshielded cosmic radiation. Mars presents a thinner atmosphere and lower sunlight (~43% of Earth's flux at the top of the atmosphere). Daytime temperatures on Mars can reach ~20 °C, but nighttime in some regions drops below −153 °C. Regolith storms further reduce insolation and can abrade solar panel surfaces. Finally, deep-space exploration encounters low-intensity, low-temperature (LILT) conditions. Solar irradiance declines with the square of distance (e.g., at Jupiter ~4% of Earth's), requiring much larger arrays, and spacecraft operate in a perpetually cold vacuum. Beyond Jupiter's ~5 astronomical units (AU), PV use to date has been limited; missions have relied on radioisotope generators, but upcoming probes aim to use solar power in these LILT environments [8–14]. We have provided a more detailed analysis of the space environment and stressors in our previous review [9].

Space PV systems are predominantly based on III-V multi-junction solar cells, particularly triple-junction architectures, due to their high-power conversion efficiency (PCE) (>30%), strong radiation tolerance, and reliable end-of-life (EOL) performance under space operating conditions. However, this performance comes at the expense of significantly higher fabrication cost compared to conventional PV technologies, which can limit scalability for emerging space platforms and large-area applications [15]. In contrast, crystalline silicon solar cells dominate the terrestrial PV market due to their scalability, and comparatively low cost [16,17]. Nevertheless, conventional single-junction silicon cells are approaching their practical efficiency limits (currently ~27-28%), nearing the Shockley-Queisser limit corresponding to the silicon bandgap [17–19], making further efficiency gains increasingly difficult through single-junction optimization alone.

To overcome this limitation, tandem solar cells (TSCs) have emerged as a promising strategy, in which multiple sub-cells with complementary bandgaps are stacked to improve spectral utilization [20,21]. In such architectures, a wide-bandgap (WBG) top cell absorbs high-energy photons (short wavelength), while transmitting lower-energy photons to a narrow-bandgap (NBG) bottom cell [21,22]. This tiered absorption approach significantly reduces thermalization losses and enables more complete use of the solar spectrum compared to a single absorber [20]. By pairing materials with suitable bandgaps, tandem designs can theoretically achieve far higher efficiencies, for example, the detailed balance limit for an ideal dual-junction TSC under 1-sun illumination is on the order of 40-42%, significantly exceeding the ~33% limit for single-junction devices [20–24]. Achieving such performance requires effective complementary absorption and careful current matching between sub-cells, which has driven significant interest in identifying suitable material systems capable of realizing high-performance TSC architectures.

Techno-economic analysis suggests that perovskite-based devices could offer reduced levelized cost of electricity (LCOE), largely due to their high projected efficiencies and low material and manufacturing costs. Fig. 1 presents the LCOE estimates derived from modeled scenarios assuming high module efficiencies, low-cost scalable fabrication, and operational lifetimes comparable to established PV technologies [25,26]. Recent cost-performance analysis further indicates that, for perovskite/silicon (Si) TSCs, the LCOE benefit can also arise from reduced balance-of-system costs, because higher-efficiency tandem

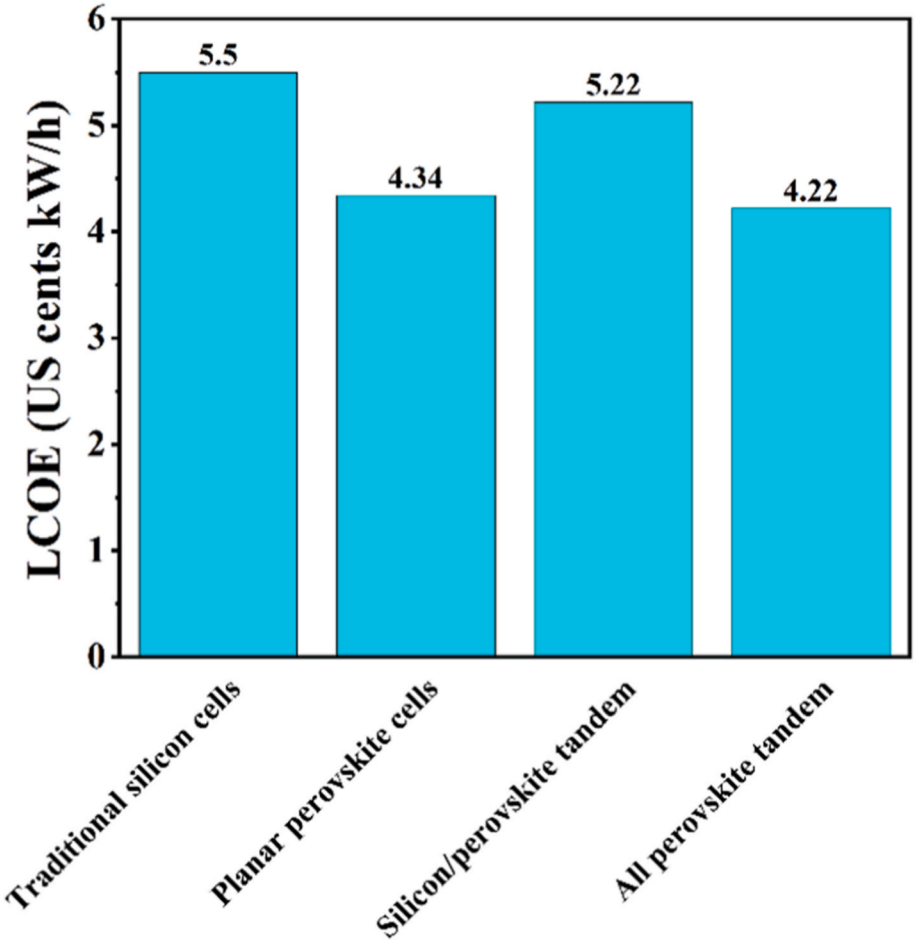

Fig. 1. *LCOE values for different solar cells* [25].

modules require less module area, mounting, cabling, installation labor, and land per unit power output [27]. Perovskite-based devices are reported to yield lower LCOE values than conventional silicon modules in such scenarios. However, these projections rely on achieving sufficient device efficiency, operational lifetime, and scalable fabrication, parameters that remain uncertain for perovskite technologies, particularly with respect to long-term stability and the absence of commercially validated lifetimes. Consequently, the reported LCOE advantages should be interpreted as conditional rather than established [25,26].

Critically, solar cells operating in space, such as LEO or the lunar surface, are exposed to a range of environmental stressors, including vacuum, intense UV irradiation, particle radiation, and temperature cycling, each of which can independently contribute to device degradation. For perovskite-based TSCs composed of a complex stack of organic, inorganic, and metallic layers, these concurrent conditions pose distinct risks that compound over time. Maintaining the structural and functional integrity of such diverse materials under overlapping stressors is one of the central challenges in adapting tandem photovoltaics for space. This review examines how space-relevant factors, including vacuum, ionizing and displacement radiation, AO, UV exposure, thermal cycling, and LILT operation, affect the longevity and performance of two-terminal (2T) perovskite TSCs. Where direct data are lacking, degradation behavior is inferred from single-junction analogues, sub-cell studies, and layer-specific studies. Unlike single-junction devices, tandem architectures rely on the coordinated operation of multiple optoelectronic layers and interfaces, each with its own failure modes under space exposure. Even localized degradation in one layer, such as interfacial delamination or charge transport layer (CTL) instability, can disrupt current matching and reduce the overall efficiency of the device. This review compiles and analyzes how individual layers, absorbers, CTLs, recombination contacts, electrodes, and encapsulants fail and their degradation pathways, identifying those most prone to failure across different stressors. To provide an integrated overview of this framework, Fig. 2 summarizes the 2T tandem device structure, the major space-relevant stressors, and their corresponding layer-level degradation effects.

To complement experimental evidence, we discuss multiscale simulation approaches that link stress-induced damage to device performance, spanning radiation energy deposition, defect formation, electrical losses, absorber/interface selection, and thermomechanical stability. Based on these insights, we discuss mitigation strategies, including composition tuning, CTL/interface passivation, radiation- and AO-resistant layers, interconnecting layer (ICL) optimization, stress engineering, and advanced encapsulation. We also use material-selection metrics, together with a weakness-stressor map, to guide practical tandem design for long-term space operation.

2. TSC fundamentals

2.1. Device architecture

TSCs are designed to overcome the efficiency limitations of single-junction photovoltaics by stacking multiple light-absorbing sub-cells, each optimized to absorb complementary parts of the solar spectrum. In such architectures, the upper sub-cell captures higher-energy photons while the lower sub-cell captures longer wavelengths, thus reducing energy loss and enhancing overall power conversion efficiency [28,29]. The way these sub-cells are electrically and optically interconnected determines the main tandem structures: that is, a series-connected 2T structure, a mechanically stacked four-terminal (4T) architecture with optically coupled but electrically independent sub-cells, and a monolithic four-terminal structure, which unites both sub-cells by a transparent conductive interface [21,30,31]. Understanding these structural distinctions is essential for evaluating efficiency potential, fabrication complexity, and reliability in applications such as space photovoltaics.

In a 2T series-connected tandem (Fig. 3a), light enters through a

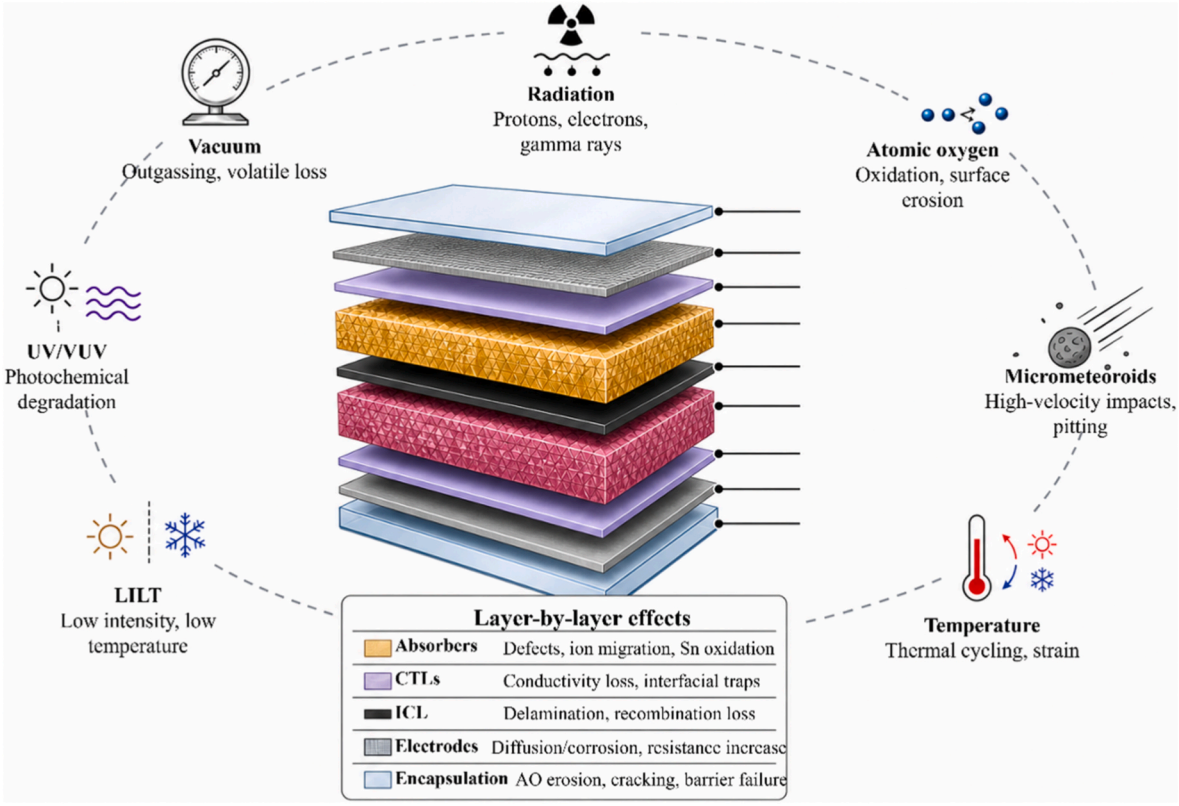

Fig. 2. Schematic illustration of a 2T perovskite tandem solar cell under space-relevant stressors. The figure also summarizes the main degradation effects in absorbers, CTLs, ICLs, electrodes, and encapsulation layers.

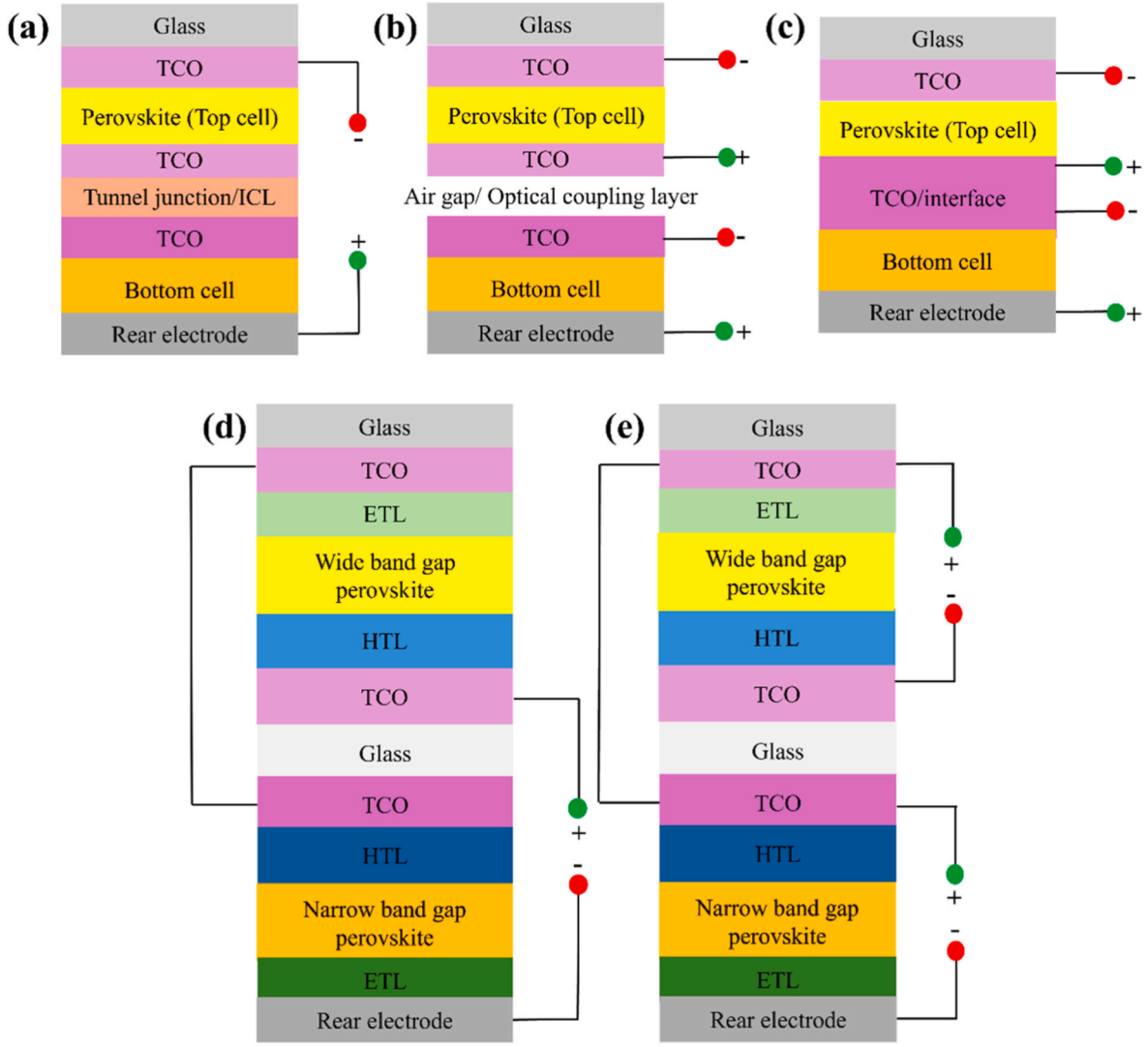

Fig. 3. Schematic illustrations of representative TSC architectures. (a) 2T monolithic tandem, where a WBG top cell and an NBG bottom cell are series-connected through a tunnel junction/ICL, enforcing current matching. (b) Four-terminal (4T) mechanically stacked tandem with optical coupling through an air gap or TCO, enabling electrically independent operation of the two sub-cells. (c) Monolithic four-terminal (4T-M) tandem, in which the sub-cells are vertically integrated and optically coupled via transparent interfaces while maintaining separate electrical contacts through buried electrodes. (d) All-perovskite 2T monolithic tandem, comprising a WBG perovskite top cell and a NBG Sn-Pb perovskite bottom cell interconnected through a recombination layer. (e) All-perovskite 4T mechanically stacked tandem, where independently contacted wide- and NBG perovskite sub-cells share optical coupling but operate at their own optimal current and voltage [30].

transparent conductive oxide (TCO)/front contact to a WBG top cell, and transmitted photons are harnessed by a narrower bandgap bottom cell. The two sub-cells are connected in series through a heavily doped n^+/p^+ ICL that provides a single current path. Device design, therefore, centers on tunnel-junction transparency/resistance and current matching across sub-cells [30]. In practical monolithic tandems, this connection is realized through an ICL that bridges the electron-transport layer (ETL) of the top cell and the hole-transport layer (HTL) of the bottom cell, while maintaining optical transparency and minimal resistive loss. Therefore, the 2T tandem design is strongly governed by current matching between the sub-cells, the optical transparency of the ICL, and the electrical resistance and stability of the recombination contact. Typical ICLs, such as indium tin oxide (ITO)/SnO_2, NiO_x/ITO, or C_{60}/atomic layer-deposited (ALD)-SnO_2, provide a combination of conductivity, transparency, and interfacial stability, supporting power conversion efficiencies exceeding 30% in perovskite/Si tandems [29].

In contrast to the 2T monolithic tandem, the 4T mechanically stacked architecture (Fig. 3b) employs optically coupled but electrically independent sub-cells, allowing each junction to operate at its own optimal voltage and current. These devices are typically coupled through an air gap or TCO which avoids current matching constraints but introduces additional optical interfaces and alignment requirements [30,32]. A monolithic 4T tandem integrates two sub-cells within a single vertical stack (Fig. 3c). Independent operation is enabled through buried TCO/electrode layers and patterned contacts. In such architectures minimizing parasitic absorption and optical losses at buried interfaces remains essential for high summed efficiency [33].

In tandem configurations, the upper sub-cell is typically perovskite owing to its tunable WBG (≈1.7-1.9 eV), which allows efficient absorption of high-energy photons while transmitting near-infrared light to the lower absorber [34]. The material's low-temperature processing and ease of forming semi-transparent electrodes make it suitable for integration onto diverse bottom-cell platforms. The lower junction is chosen to complement the transmitted spectrum, commonly employing Si (~1.1 eV), copper indium gallium selenide (CIGS) (~1.0–1.2 eV), narrow-gap Sn-Pb perovskites (~1.2 eV), or III-V semiconductors (GaAs, InGaAs, Ge) [35,36].

In the context of all-perovskite TSCs, both the 2T and 4T

configurations are most commonly adopted owing to their effective balance between device efficiency and fabrication practicality. In the 2T monolithic structure (Fig. 3d), a WBG perovskite top sub-cell (≈1.75 eV), such as lead perovskites, is stacked above an NBG Sn-Pb perovskite bottom sub-cell using an ICL that simultaneously facilitates charge recombination and optical transmission. In this configuration, both sub-cells were fabricated on opposite sides of a double-sided ITO substrate. In contrast, the 4T mechanically stacked structure (Fig. 3e) places two independently contacted sub-cells on either side of the same transparent electrode, enabling each to operate at its own optimal current and voltage [30]. Together, these device architectures demonstrate the design versatility of all-perovskite tandems and underscore their potential for scalable, high efficiency multijunction photovoltaics. Among the tandem architectures discussed above, this review focuses specifically on 2T perovskite TSCs because their monolithic series-connected design offers a compact and technologically relevant platform for evaluating space-oriented efficiency and reliability.

2.2. Bandgap tuning for AM0 spectrum

The effective use of high-efficiency TSCs in space demands accurate optimization with the Air Mass Zero (AM0) solar spectrum. AM0 defines extraterrestrial irradiance, which is fundamentally different from the terrestrial Air Mass 1.5 Global (AM1.5G) standard. These differences are significant to understand bandgap selection and current matching in tandem designs. The total integrated power density contained in the AM0 spectrum is much greater, about 1366.1 W/m^2, than the 1000 W/m^2 AM1.5G standard. More importantly, there is no atmospheric filtering of the AM0 spectrum, so the flux of high-energy (ultraviolet and blue) photons reaching the device surface is greatly increased, directly affecting the bandgap tuning needed to build tandem devices [9,37]. Under AM0, a stack with two junctions will have the short-circuit current density of the top cell, ($J_{sc,Top}$) increasing disproportionately compared to the bottom cell, ($J_{sc,Bottom}$). As a result, to achieve current matching conditions ($J_{sc,Top} = J_{sc,Bottom}$) which are mandatory in monolithic, 2T devices, the necessary optimum top-cell bandgap ($E_{g,Top}$) has to be shifted towards smaller values than those suggested to operate with AM1.5G on the landside, or the top cell has to be fabricated much thinner. This has to be adjusted to avoid the top cell severely limiting the total current flow, which is restricted by the lower spectral response of the bottom cell in the longer wavelengths [38].

For dual-junction TSCs, detailed-balance calculations show that the optimum bandgap combination depends strongly on the illumination spectrum. For ideal 2T TSCs, the efficiency contour maps show that under AM0 illumination (Fig. 4a), the optimized bottom/top bandgap pair is approximately 0.90/1.58 eV, giving a theoretical efficiency limit of ~42.3%. Under AM 1.5G illumination (Fig. 4b), the optimized combinations shift to approximately 0.95/1.60 eV and 1.12/1.72 eV, with corresponding limits of ~45.5% and ~44.9%, respectively. This indicates that the commonly discussed optimum bandgap combination for TSCs is not universal but is strongly dependent on the incident solar spectrum [39].

Under AM0 illumination, bandgap tuning should be considered together with the spectral fitting introduced by the front optical stack. Although AM0 contains a stronger ultraviolet component than terrestrial AM 1.5G, practical space photovoltaic modules may require UV-stable coatings or UV-filtering layers to suppress photon-induced degradation in perovskite absorbers and CTLs [40,41]. Therefore, the short-wavelength contribution to photocurrent may be partly reduced depending on the optical design. However, AM0-based optimization remains distinct from AM 1.5G optimization, because the extraterrestrial spectrum is not modified by atmospheric absorption, especially H_2O-related absorption bands that reduce near-infrared photon flux under terrestrial conditions [39]. These additional near-infrared photons can enhance the bottom-cell photocurrent and modify current matching in 2T tandem architectures [39,42]. Thus, AM0 bandgap tuning should not be viewed only as a response to UV exposure, but as a coupled problem involving spectrum-dependent current matching, UV-stability management, and long-wavelength photon utilization.

2.3. Interfaces and CTLs relevant to stability

Interfaces and CTLs play a key role in the stability of perovskite TSCs. The ETL and HTL are not just paths for charge movement; they control energy alignment, reduce unwanted charge loss, and protect the perovskite from chemical damage. During long exposure to light and heat, these interfaces often become weak points, causing voltage loss and lower efficiency. Understanding and improving the contact between the perovskite and the CTLs is therefore essential for keeping the device stable in both space and normal environments [43–45]. A study by Aalbers et al. emphasized that non-radiative losses originate predominantly from the perovskite/ETL interface rather than the HTL side, with the C_{60} layer contributing over 100 mV to the total voltage loss [46]. By contrast, the 2PACz–perovskite interface exhibited negligible recombination losses. The authors also established a strong correlation between the sub-bandgap external quantum efficiency (EQE) defect signal and $\Delta V_{non\text{-}rad}$, confirming that minimizing these interfacial defects through effective passivation is critical for achieving high and stable V_{oc} values [46]. Their work is consistent with the broader view that how energy levels line up at the interface controls recombination. If the ETL and

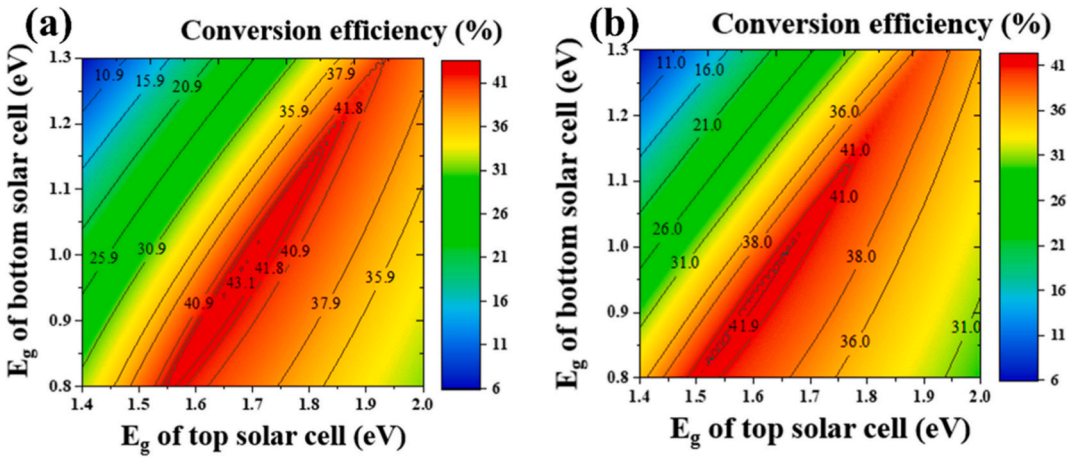

Fig. 4. Detailed-balance efficiency contour plots for ideal two-terminal double-junction TSCs under (a) AM0 and (b) AM1.5G illumination, plotted as a function of bottom-cell and top-cell bandgaps [39].

perovskite are mismatched, more charge carriers get trapped and recombine, causing a loss in voltage. Good passivation and energy alignment reduce these traps and improve both V_{oc} and device lifetime [47].

In addition to energy-level matching, chemical interactions at the CTL/perovskite interface strongly affect stability. Although PEDOT:PSS remains more commonly employed in Sn-based NBG perovskite solar cells (PSCs), NiO_x has attracted attention as an inorganic HTL because of its improved thermal robustness and long-term stability in mixed Sn-Pb devices. For example, Han et al. reported low-temperature processed NiO_x as an HTL for Sn-Pb solar cells, achieving stable device performance and 95% efficiency retention after 102 days [48]. However, the use of NiO_x in Sn-Pb NBG PSCs remains limited by two interfacial issues: the energy-level mismatch between NiO_x and the Sn-Pb perovskite, and the redox reaction between $Ni \geq^{3+}$ species in NiO_x and Sn^{2+} in the absorber. Zhang et al. addressed these limitations by introducing a 4-aminobenzenesulfonic acid interlayer at the NiO_x/Sn-Pb perovskite interface. The interlayer formed an oriented molecular dipole that improved the valence-band alignment of NiO_x, while its chemical interaction with NiO_x and the perovskite suppressed $Ni^{\geq 3+}$-induced Sn^{2+} oxidation. As a result, the device efficiency increased from 14.56% to 17.4%, with more than 90% of the initial PCE retained after 480 h under 1-sun illumination in N_2 [49]. These results are consistent with the findings of Bian et al., who showed that Ni^{3+} can oxidize Sn^{2+} at the interface generating defect sites and accelerating recombination losses. [50]. Pre-reducing Ni^{3+} with ascorbic acid suppressed this redox process, enhancing both V_{oc} and stability [50]. These studies indicate that NiO_x is a promising but chemically sensitive HTL for Sn-containing NBG sub-cells. Optimizing both the energetic alignment and NiO_x/Sn^{2+} interfacial redox stability is therefore vital for sustaining high efficiency and long-term stability in perovskite TSCs.

2.4. Perovskite compositions and structural design for stable tandem operation

Perovskite composition is a key stability factor in TSCs because it controls the bandgap, crystal phase, defect formation, and ion-migration behavior of the absorber. In WBG top cells, mixed I/Br perovskites are commonly used to obtain the higher bandgap required for efficient tandem current matching. However, these mixed-halide compositions can become unstable when iodide and bromide redistribute within the lattice, forming iodide-rich lower-bandgap regions and bromide-rich domains. This halide segregation creates local energetic disorder and introduces sub-bandgap trap states. The iodide-rich regions can trap photogenerated carriers and obstruct charge collection, leading to a pronounced loss in J_{sc}. In 2T tandem operation, such bandgap and recombination changes are especially important because the top and bottom sub-cells are electrically coupled, so instability in the WBG perovskite can directly affect current matching and overall tandem output. Therefore, controlling mixed-halide composition and suppressing halide redistribution are central requirements for stable perovskite tandem operation [51].

A-site cation engineering is another important compositional strategy for improving the structural stability of perovskite absorbers. In the ABX_3 lattice, the A-site cation influences the tolerance factor, phase formation, crystallinity, and the stability of mixed-halide compositions. The incorporation of Cs into FA/MA-based perovskites has been shown to produce triple-cation films with improved phase purity, higher crystallinity, and better reproducibility compared with MA/FA-only compositions [52]. For tandem-relevant WBG absorbers, FA/Cs mixed-cation lead mixed-halide perovskites provide a suitable bandgap near 1.7-1.8 eV while improving compositional photostability, making them suitable for top-cell operation in tandem architectures [53]. Further extension to multi-cation systems, including small inorganic Rb^+ cations, shows that carefully designed A-site "cation cascades" can tune lattice stability, increase defect tolerance and improve material quality in complex mixed-cation/mixed-halide perovskites [54]. Therefore, A-site cation selection directly affects phase stability, halide distribution, and the reliability of WBG perovskite absorbers.

Ion migration is widely recognized as one of the major intrinsic instability pathways in metal-halide perovskites, especially under illumination, heat, and internal electric fields. Low-dimensional perovskite phases have been reported as an effective strategy to mitigate this issue because their layered structures can interrupt the continuous 3D migration pathways present in conventional perovskite lattices. For example, Ruddlesden-Popper-type low-dimensional perovskites showed suppressed ion migration under both dark and illuminated conditions, while grain-boundary studies indicate that these regions can provide lower-energy migration pathways than the bulk [55,56]. Reduced-dimensional or quasi-2D perovskites have also been shown to limit iodide migration and reduce ion-migration-induced interfacial degradation [57]. These findings suggest that controlled low-dimensional incorporation can improve tandem absorber stability by limiting grain-boundary ion transport.

Alongside WBG top-cell stabilization, the composition of the NBG bottom absorber is equally critical in all-perovskite TSCs. Mixed Sn-Pb perovskites are important for all-perovskite TSCs because their narrow bandgap enables near-infrared absorption and current matching with the WBG top sub-cell [58]. However, Sn-Pb absorbers are less stable than Pb-based perovskites due to easy Sn^{2+} oxidation to Sn^{4+} and the different crystallization behavior of Sn- and Pb-based precursors, which can increase defect formation and non-radiative recombination [59]. Recent studies show that molecular strategies can regulate Sn-Pb crystallization and raise the Sn^{2+} oxidation barrier, improving film quality and device stability [59,60]. Therefore, stabilizing the Sn-Pb NBG absorber is essential for maintaining bottom-cell carrier collection and current balance in 2T tandem operation.

3. Degradation under individual space stressors

3.1. Ionizing and displacement radiation

In space environments, perovskite TSCs are subjected to a broad spectrum of ionizing and displacement radiation that collectively determine their operational durability. Ionizing radiation primarily deposits energy through electronic excitations, leading to charge buildup and interface trap formation, while displacement radiation imparts momentum to lattice atoms, creating vacancies and interstitials that disrupt the crystal structure. The multilayer configuration of tandem architecture makes them particularly vulnerable to these effects, as damage may accumulate differently across each sub-cell and ICL. The principal radiation types influencing perovskite tandems in space include gamma rays, high-energy electrons, protons, neutrons, and heavy ions.

Gamma-ray studies comparing mixed tin-lead (Sn-Pb) and pure lead (Pb) PSCs provide valuable insight into how ionizing radiation influences absorber materials commonly used in tandem architectures, where the WBG Pb-based perovskite usually serves as the top cell and the NBG Sn-Pb alloy as the bottom cell. In a comparative study. Zhang et al. examined $CH_3NH_3Pb_{0.7}Sn_{0.3}I_3$ and $CH_3NH_3PbI_3$ devices under Co_{60} gamma irradiation. They reported that the PCE of the Sn-Pb-based PSCs decreased from 15.65% to 10.78% after 0.75 kGy and to 5.17% after 10 kGy, corresponding to relative losses of 31% and 67%, respectively. In contrast, the PCE of the Pb-based PSCs decreased from 20.20% to 10.49% after 0.75 kGy and to 1.95% after 10 kGy, corresponding to larger losses of 48% and 90%, respectively. To rationalize this device-level degradation trend, the authors further examined the irradiated absorber films. Fig. 5a-d shows scanning electron microscopy (SEM) analysis comparing the pristine films and those exposed to 10 kGy reveals that Sn-Pb retains its compact crystalline grains. In contrast, the Pb film undergoes extensive decomposition and grain-boundary formation, indicating disrupted carrier pathways. The study attributed the

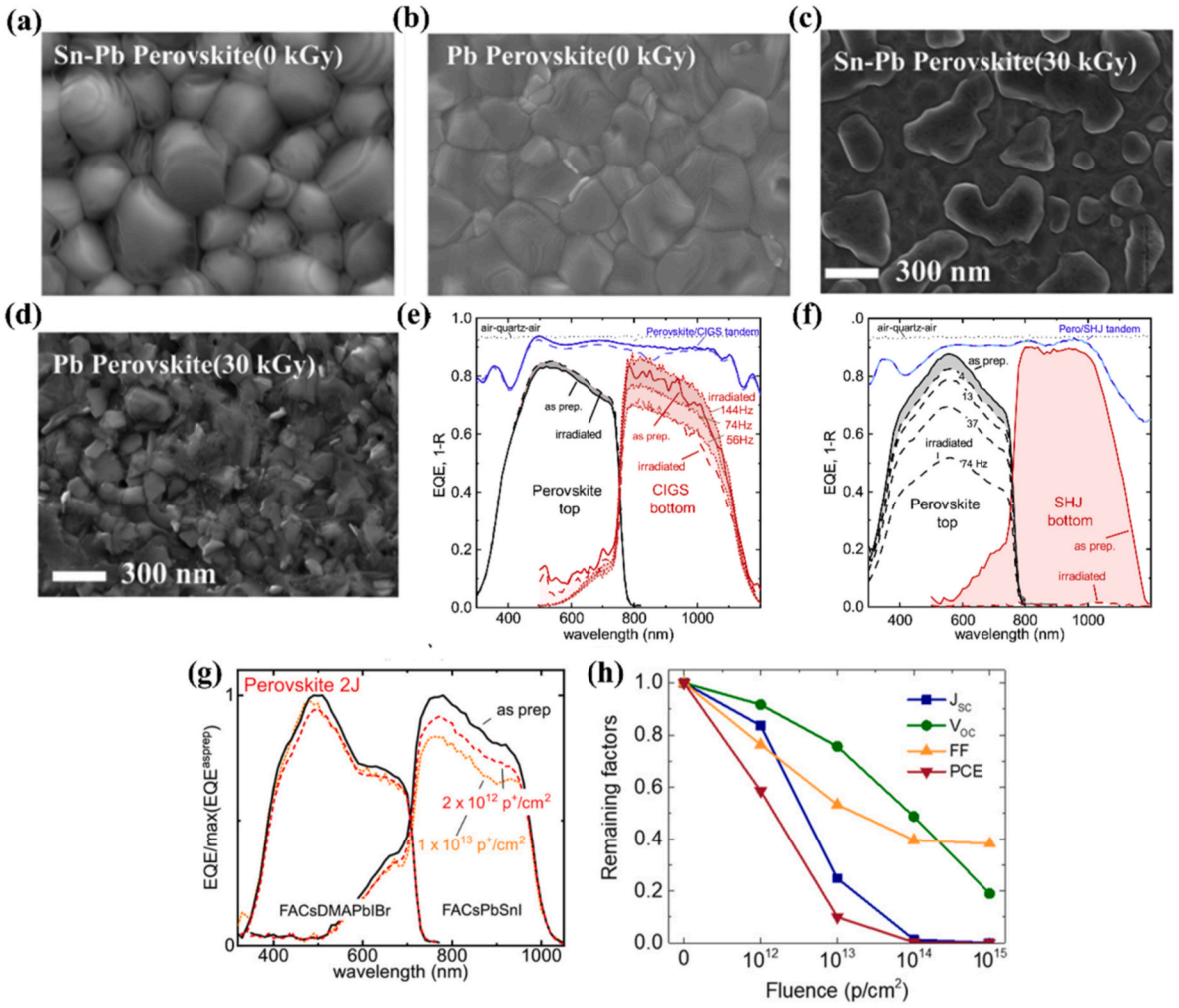

Fig. 5. Irradiation response of tandem-relevant films and sub-cells. (a,b) SEM of Sn–Pb mixed and Pb-based perovskite films at 0 kGy; (c,d) corresponding films after γ-ray irradiation to a total ionization dose of 30 kGy (scale bar: 300 nm) [61]. (e,f) EQE of the perovskite top and CIGS or SHJ bottom sub-cells before (solid) and after proton irradiation (dashed); measurements used 74 Hz chopping with LED light bias, with additional chopper-frequency and bias conditions as indicated. TSC reflectance is shown in blue, and the air–quartz–air encapsulation reflectance is shown as a dotted black line [62]. (g) Normalized EQE change for the perovskite two-junction TSC, plotted as $EQE_{max}(EQE_{as\text{-}prepared})$, under proton fluence [63]. (h) Remaining factors of the organic photovoltaic devices after 150 keV proton irradiation [64].

improved radiation stability of Sn-Pb perovskites to reduced formation and migration of iodine-related defects and the predominance of shallow rather than deep trap states, which limits non-radiative recombination and helps preserve carrier transport under gamma irradiation. These results indicate that Sn-Pb perovskites demonstrate superior tolerance specifically to gamma-ray irradiation relative to pure Pb-based compositions, making them a strong candidate for the radiation-hard sub-cell in TSCs intended for ionizing environments such as space [61].

Having surveyed perovskite absorbers, we turn to crystalline silicon, which exhibits a distinct dose response dominated by current and lifetime losses. Under ^{60}Co irradiation from 1 to 20 kGy, mono-crystalline Si cells showed dose-dependent declines in I_{SC} and efficiency, while V_{OC} decreases modestly and fill factor (FF) remains comparatively stable. Spectral photocurrent drops most in the blue region (400–500 nm), corresponding to absorption near the cell surface, pointing to defect formation near the surface at lower doses, with broader spectral loss at the highest dose. Minority-carrier lifetime consistently decreases, evidencing enhanced recombination. These observations link gamma-induced defects to reduced diffusion length and performance [65].

Extending the discussion from inorganic absorbers to organic systems, organic solar cells exhibit a fundamentally different response to ionizing radiation due to their soft molecular structure and interface-dominated transport. In P3HT:PCBM-based devices, gamma irradiation primarily influences the polymeric transport layer and donor–acceptor interface rather than causing severe bulk structural damage. Yağci et al. reported that under low-dose Co [60] gamma irradiation (~40 Gy), organic solar cells show improved performance, with ~40% enhancement in J_{sc} and ~49% increase in PCE compared to non-irradiated devices [66]. This improvement is attributed to radiation-induced modifications in the PEDOT:PSS layer, where increased surface roughness enhances interfacial charge extraction, while increased optical transparency allows greater photon transmission into the active layer. Additionally, only minor structural changes occur in the polymer without significant degradation, indicating tolerance to low ionizing doses alongside improved interfacial properties [66].

Among the absorber systems compared, both crystalline silicon and perovskite solar cells exhibit performance degradation under gamma irradiation, primarily driven by radiation-induced defect formation that enhances recombination and reduces carrier lifetime. In contrast, organic solar cells display a fundamentally different response, where low-dose gamma irradiation can lead to performance enhancement rather than degradation due to modifications in interfacial and transport-layer properties. In a tandem configuration, this contrast

suggests that while inorganic sub-cells are susceptible to cumulative radiation damage, organic sub-cells may temporarily benefit from low-dose ionizing environments through improved charge extraction and optical properties, although their stability at higher radiation doses remains uncertain.

While gamma irradiation primarily introduces ionizing damage, it does not capture how these materials behave under displacement-driven stress. To address this complementary degradation pathway, we next examine their response to proton irradiation, where atomic displacements dominate. As reported by Lang et al., the two monolithic tandem architectures show markedly different behavior under 68 MeV proton irradiation [62]. The perovskite/CIGS TSC remains comparatively stable at a fluence of 2×10^{12} p/cm^2, retaining about 86% of its initial AM0 power output, which decreases from 202 to 173 W/m^2. The J_{sc} changes only slightly from 20.0 to 19.4 mA/cm^2, while modest reductions in V_{oc} and fill factor account for the overall loss. The external quantum efficiency shown in Fig. 5e indicates that the perovskite top sub-cell remains essentially unaffected, with a small increase in its integrated response, whereas the CIGS bottom sub-cell exhibits a moderate reduction that is consistent with added recombination in the CIGS layer and at the NiO recombination contact. In contrast, the perovskite/silicon heterojunction (SHJ) tandem is highly vulnerable. Its AM0 power output drops from 257 to 4 W per m^2, which corresponds to only about 2 percent of the original value. This severe degradation is driven by the collapse of the SHJ, where the short circuit current decreases from 21.5 to 0.30 mA/cm^{2,} and the EQE shown in Fig. 5f falls from approximately 90 percent to about 1.5 percent. The perovskite top cell shows only a small change in its integrated photocurrent, confirming that the silicon sub-cell is the dominant radiation-sensitive component in this tandem configuration [62].

Another study led by Lang et al. evaluated the proton tolerance of all-perovskite monolithic tandems, offering a direct contrast to the hybrid tandems discussed earlier [63]. When exposed to 68 MeV protons at fluences up to 1×10^{13} cm^{-2}, the tandems preserved about 97% and 94% of their initial output at the two tested doses (Fig. S1). The EQE evolution confirms that the WBG top sub-cell remains essentially unchanged. In contrast, the NBG bottom sub-cell experiences only a modest reduction, with integrated EQE falling to roughly 90% and 83% at the lower and higher fluences (Fig. 5g). Importantly, the authors show that the perovskite absorbers themselves do not accumulate radiation-induced defects, as both bare high- and low-gap films retain their photoluminescence (PL) and quasi-Fermi-level splitting (QFLS) after irradiation. This behavior demonstrates that the performance loss does not originate in the absorbers but is instead linked to changes within the recombination contact (C_{60}/aluminum-doped zinc oxide (AZO)/ITO/PEDOT:PSS), which the study identifies as the weakest region of the device under proton exposure. Subtle irradiation-induced modifications at this interface, rather than bulk damage, therefore, governs the small efficiency decline in the fully perovskite TSCs [63].

Under 150 keV proton irradiation, organic PV devices exhibit a clear fluence-dependent degradation in performance, as summarized in Fig. 5h, where all key parameters decrease progressively with increasing proton exposure. The dominant loss originates from a strong reduction in J_{sc}, indicating that photocurrent generation and collection are primarily affected. Importantly, this decline is not associated with significant changes in optical absorption at low to moderate fluence but instead arises from radiation-induced trap states within the active layer, which enhances trap-assisted recombination and reduces charge carrier mobility. Transient measurements further confirm an increase in recombination-related losses, consistent with the formation of shallow traps. At the molecular level, proton irradiation induces conformational changes in the polymer backbone and promotes cross-linking within the active layer, leading to increased energetic disorder and reduced solubility. Despite this degradation, the study reports that organic solar cells retain a higher fraction of their initial performance compared to conventional III-V technologies under similar irradiation conditions, highlighting a distinct balance between degradation mechanisms and relative radiation tolerance [64].

To date, experimental radiation-hardness studies of perovskite TSCs remains largely restricted to proton irradiation (e.g., the work by Lang et al. on perovskite/Si and all-perovskite architectures [62,63]), whereas neutron, electron, and heavy-ion irradiation have only been systematically examined for single-junction perovskite films and devices. As a result, the radiation response of perovskite TSCs to these additional particle types remains essentially unexplored, representing a clear gap in the current literature.

3.2. Vacuum and outgassing

After reviewing the radiation response of TSCs, it is also necessary to consider how vacuum conditions affect device stability, even though dedicated studies on complete tandem structures remain limited. Evidence from single-junction perovskite solar cells demonstrates a strong pressure dependence in degradation rate. When the operating pressure is reduced from 9×10^4 Pa to 5×10^3 Pa, the triple cation absorber decomposes nearly ten times faster under illumination, with the T_{80} lifetime dropping from about 109 h to 8.5 h. This behavior is clearly reflected in X-ray diffraction (XRD) results shown in Fig. 6a and b. In Fig. 6a, the characteristic perovskite layer diffraction peak systematically weakens as pressure decreases, showing the loss of the crystalline perovskite phase. Fig. 6b further quantifies this transformation by showing a pronounced increase in the relative peak areas of decomposition products such as PbI_2, metallic Pb, and non-photoactive δ phases at lower pressures. These phase changes originate within the perovskite absorber itself and reflect the removal of volatile species under vacuum. Together, these observations indicate that vacuum-induced volatile loss and the resulting structural breakdown of the absorber are likely to contribute significantly to degradation pathways in perovskite-based TSCs [67].

Across both 3D perovskite solar cells and 2D layered perovskite structures, vacuum exposure consistently accelerates chemical and structural degradation by promoting the loss of volatile species and altering the perovskite composition. In the 2D perovskite study, this trend is directly reflected in the rise of metallic lead during vacuum exposure, where the metallic Pb fraction steadily increases over time from X-ray photoelectron spectroscopy (XPS) results (Fig. 6c), confirming vacuum-induced decomposition of the perovskite lattice [68]. The 3D perovskite work reports a similar response under operando vacuum testing, where devices were operated under a vacuum pressure of 5×10^{-1} Pa. Under these conditions, they reported pronounced lattice shrinkage and phase segregation in the MAFA perovskite layer, along with a strong increase in the relative population of small crystalline domains during vacuum operation. The normalized counts of 5 nm crystals increased from 3 at 0 min to 670 after 120 min, while the counts at 10 nm increased from about 10 to 275 over the same period. This morphology evolution was linked to the formation of pinholes lowering shunt resistance and contributing to the decreases in V_{oc} and FF [72]. Consistent with this morphology-driven degradation, Ahn et al. used SEM to show that pristine perovskite films exposed to high vacuum developed increased porosity, crack-like surface features, and rougher morphology, with the RMS roughness increasing from 25.0 nm before vacuum to 81.2 nm after vacuum (Fig. S2) [73].

Within full device stacks, the perovskite/HTL interface is identified as the most vulnerable region under vacuum because changes in composition and ion migration are concentrated at this contact, amplifying voltage losses. These combined observations indicate that vacuum-driven outgassing is a central factor linking the structural, compositional, and interfacial instabilities reported in both studies [68,72]. Given that tandem top cells rely on similar mixed-cation perovskite absorbers and the same sensitive interfacial layers, the vacuum-induced outgassing and structural breakdown observed in single-junction devices are likely to represent key degradation routes in the tandem

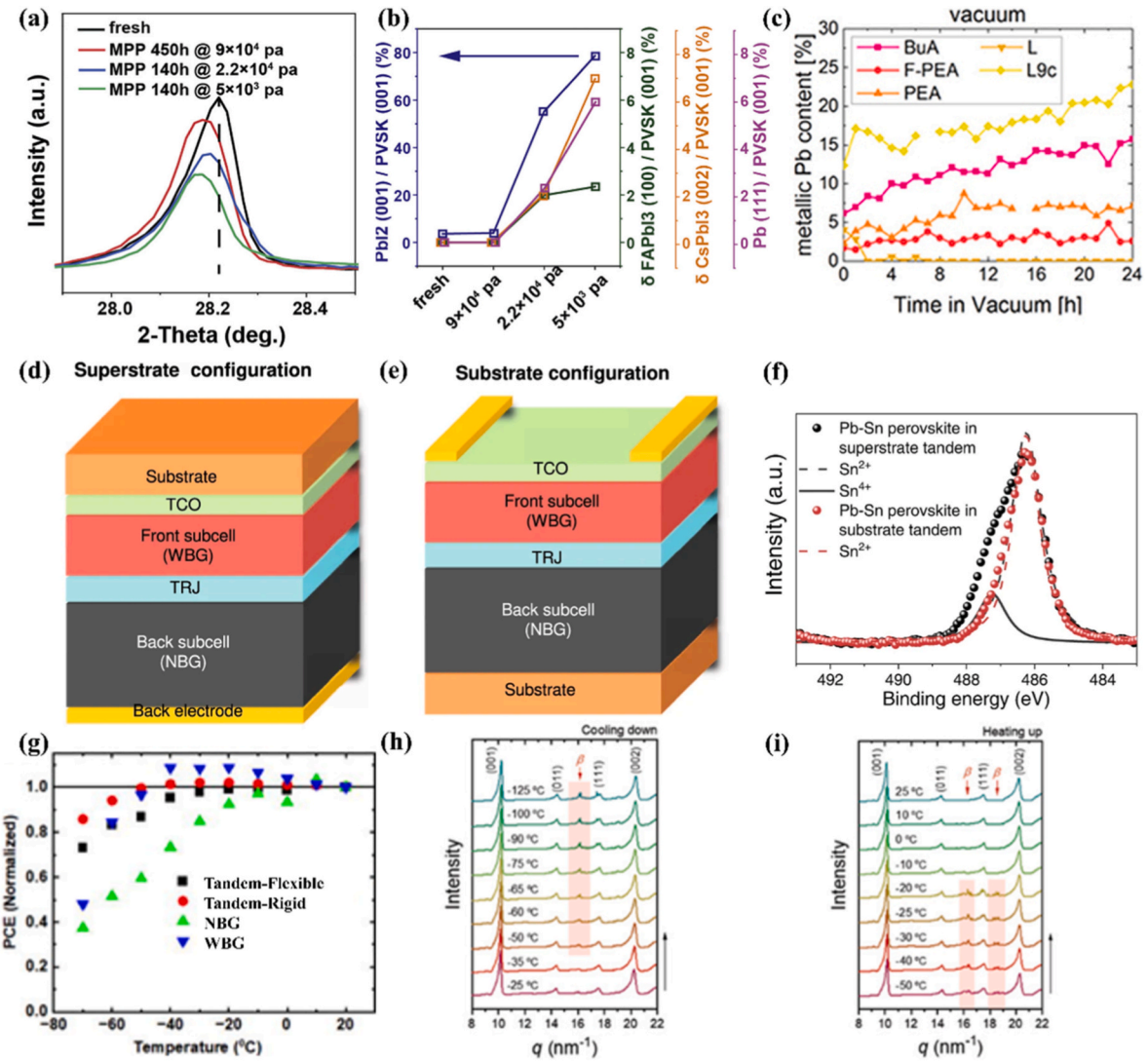

Fig. 6. Structural, chemical, and device-level evolution of perovskite solar cells and all-perovskite TSCs under operation and aging. (a) XRD comparison of the (002) reflection for freshly prepared versus aged PSCs; the OHP-related peaks shift to lower 2θ indicates the operation-induced change in OHP composition. (b) Pressure-dependent transformation of the OHP film during operation, quantified as the ratios of decomposition/non-photoactive phases to the OHP phase using representative XRD peak areas [67]. (c) Time evolution of metallic Pb fraction (relative to total Pb) for BuA, F-PEA, PEA, L, and L9c during vacuum exposure [68]. (d,e) Design and fabrication workflow for substrate configuration all-perovskite TSCs, together with the device architectures for superstrate and substrate-configured TSCs. (f) Sn $3d_{5/2}$ XPS spectra of NBG perovskite layers in superstrate- and substrate-configured TSCs after dry-air aging (20 h and 200 h, respectively) [69]. (g) Temperature-dependent normalized power conversion efficiency (PCE) for NBG, WBG, tandem-flexible, and tandem-rigid PSC devices [70]. (h,i) Representative 1D profiles for the cooling and heating processes [71].

configuration as well.

The extent of vacuum-related outgassing also depends on A-site cation composition. Shi et al. identified volatile decomposition products from MA^- and FA^- containing precursors, including CH_3I, CH_3Br, NH_3, HCN, and HI, while CsI showed no obvious outgassing contribution [74]. CsFAMA cells also released only about one-fifth of the decomposition products detected from FAMA cells, indicating that Cs incorporation can suppress volatile outgassing. Therefore, the qualitative outgassing tendency can be described as MA/FA-rich compositions > Cs-containing mixed-cation compositions> fully inorganic Cs-based compositions. This suggests that reducing volatile organic-cation content and incorporating Cs may help mitigate vacuum-induced degradation in perovskite tandem top cells [74].

Encapsulation provides a complementary route to limit volatile loss, provided that it forms a pressure-tight barrier rather than only a moisture barrier. Shi et al. showed that polymer/glass blanket encapsulation suppresses volatile products such as CH_3I, CH_3Br, and NH_3 from MA-containing mixed-cation PSCs, while polyisobutylene (PIB) or polyolefin (PO) polymer layers alone were insufficient without a cover glass [74]. Mariani et al. further emphasized that encapsulants should not only block external moisture/oxygen ingress but also constrain volatile outgassing. They therefore proposed glass/PIB/glass and glass/PIB: hexagonal boron nitride (h-BN)/glass as pressure-tight encapsulation structures [75]. Therefore, for low-pressure or vacuum-like environments, pressure-tight polymer/glass or glass/polymer/glass encapsulation based on PIB, PO, or PIB:h-BN barriers are more relevant than polymer-only encapsulation.

In contrast to perovskites, where vacuum directly accelerates intrinsic chemical decomposition through volatile loss, organic solar cells exhibit a different response to low-pressure conditions. Experimental studies combining stratospheric balloon flight (real near-space conditions) and controlled vacuum testing show that organic devices can remain operational under reduced pressure, with no clear evidence of intrinsic active-layer degradation. Instead, performance loss is

primarily linked to mechanical and interfacial instability, particularly failure of encapsulation under rapid depressurization, which leads to delamination or fracture of protective layers. Devices with more robust encapsulation demonstrate improved stability, emphasizing that degradation is dominated by packaging reliability rather than material decomposition. Overall, these results indicate that vacuum itself is not a primary degradation driver in organic solar cells, and that observed performance losses are more strongly governed by encapsulation integrity and combined environmental stressors [76].

3.3. AO

In addition to vacuum effects, the near-Earth environment exposes TSCs to energetic AO, introducing a further oxidation-driven degradation pathway relevant to LEO operation. Ground-based AO testing can provide useful accelerated evaluation, but its relevance to LEO depends on how closely the test environment is defined and controlled. The NASA atomic oxygen testing protocol notes that AO facilities can be broadly divided into plasma-based systems and directed beam systems. Directed hyperthermal AO beams better reproduce the neutral, directional oxygen-atom impact relevant to LEO, where AO reaches spacecraft surfaces with an energy close to 5 eV. In contrast, plasma-based systems can include additional components such as ions, excited-state species, and UV/vacuum ultraviolet (VUV) radiation. Therefore, AO fluence, flux, oxygen-atom energy, sample temperature, exposure geometry, and the presence of ions or UV/VUV radiation should be specified when relating laboratory AO results to LEO exposure [77].

In the absence of direct AO data for TSCs, we refer to oxygen/air stability studies as an indirect indicator of which layers are most susceptible to oxidation, with the understanding that AO in LEO represents a more aggressive limit case of the same underlying chemistry. Wang et al. demonstrated that oxygen degradation in all-perovskite TSCs originates in the Sn-Pb NBG sub-cell, and the severity of this reaction depends on the device structure [69]. In the superstrate configuration, shown in Fig. 6d, the stack is built on a transparent substrate, and the NBG layer is deposited last at the top, leaving it directly exposed to oxygen. In contrast, the substrate configuration, shown in Fig. 6e, reverses the deposition sequence so that the Pb-Sn NBG layer is fabricated first at the bottom of the device and then buried beneath the recombination junction and WBG sub-cell. This physical burial markedly suppresses oxygen access. Fig. 6f captures the oxygen effect clearly: the superstrate device develops a pronounced Sn^{4+} peak after 20 h in dry air, while the substrate device shows almost no Sn^{4+} even after far longer exposure. These results confirm that the oxygen-sensitive NBG layer is the critical degradation site and that the substrate architecture provides an effective mitigation route [69]. Overall, the pronounced sensitivity of the Sn-Pb NBG sub-cell to oxygen in the study by Wang et al. suggests that AO in near-Earth orbits could trigger a similar $Sn^{2+} \rightarrow Sn^{4+}$ oxidation pathway. However, this comparison must be made carefully, as ambient O_2 and AO differ markedly in energy and surface reactivity. Ambient oxygen drives relatively slow chemical oxidation, whereas AO is far more energetic and can induce both oxidation and physical erosion [78]. Thus, oxygen-exposure studies reveal which layers are vulnerable, but they cannot be directly equated to the severity or mechanisms of AO damage.

Insights from single-junction PSCs offer a meaningful indication of how AO may interact with the individual layers that also appear in TSCs. A study by Seid et al. on p-i-n perovskite cells has shown that AO primarily attacks surface and interfacial components rather than the perovskite bulk, with the most severe damage occurring in ultrathin organic passivation layers such as phenethylammonium iodide (PEAI) [78]. These studies reveal that AO can rapidly dismantle the 2D interlayer, generate lead-iodide-rich surface phases, reduce charge-extraction efficiency, and propagate laterally beneath metal contacts through damaged surface domains. Although the absolute rates and magnitudes cannot be directly mapped to TSCs, the layer-specific vulnerabilities, including the susceptibility of organic surface treatments, the relative robustness of deeper absorber regions, and the effectiveness of inorganic encapsulation such as thin SiO coatings, are directly relevant for TSC design. In addition, space-exposure studies such as Materials International Space Station Experiment-16 (MISSE-16) have shown that common polymeric materials, including PET films, polyimides, and other films often used as encapsulants or substrates, undergo significant AO-induced erosion and surface roughening in LEO, which can reduce optical transmission and compromise long-term mechanical durability. These findings further underscore that AO stability in space cannot rely on conventional polymer layers and may require AO-resistant coatings or nanocomposite barriers such as polyhedral oligomeric silsesquioxane (POSS)-enhanced materials to preserve optical and structural integrity. Therefore, single-junction AO investigations provide a practical basis for anticipating which tandem interfaces, surface chemistries, and contact structures may require reinforcement when operating in AO-rich LEO conditions [78,79]. Overall, the emerging evidence suggests that the AO-driven vulnerabilities observed in single-junction PSCs will likely manifest in analogous surface and interfacial layers within TSCs unless specifically reinforced.

3.4. Thermal cycling

While AO primarily affects surface chemistry and encapsulation integrity, temperature variations introduce a different set of challenges, warranting a detailed discussion of thermal effects. Space operation subjects solar cells to various thermal challenges, including low-temperature exposure, high-temperature stress, and thermal cycling. In perovskite-based devices, these temperature variations should also be considered in relation to the intrinsic structural phase-transition temperatures of the absorber, which are strongly composition-dependent. Since different perovskite compositions exhibit different phase-transition windows, crossing these temperatures can alter lattice parameters, thermal expansion behavior, band structure, optical response, phonon structure, and charge transport. For example, Keshavarz et al. showed that $MAPbI_3$, $MAPbBr_3$, δ-$FAPbI_3$, and $FAPbBr_3$ exhibit distinct temperature-dependent thermal-expansion and phase-transition behavior, including negative thermal expansion in δ-$FAPbI_3$ and multiple sharp transitions in $FAPbBr_3$ [80]. Therefore, in TSCs, the operating or cycling temperature range should be compared with the phase-transition window of the specific perovskite composition, since phase-transition-induced lattice changes may contribute to interfacial strain and temperature-dependent changes in bandgap or carrier transport. Perovskite-based devices, ranging from single-junction absorbers to monolithic TSCs, exhibit temperature-dependent behavior that is particularly relevant for space operation.

In their study, Datt et al. worked with four perovskite-based architectures: a tandem-rigid PSC, a tandem-flexible PSC, and two single-junction devices comprising a WBG PSC and an NBG PSC, enabling a direct comparison of thermal stability across device types [70]. Their low-temperature measurements, presented in Fig. 6g, show normalized PCE from +20 °C to −70 °C and reveal that the NBG device is the most susceptible to cooling, losing nearly two-thirds of its initial efficiency. The WBG device retains roughly half, while the tandem-flexible and tandem-rigid configurations preserve about 70% and 85%, respectively. The degradation in single-junction PSCs originated from the decrease in the FF, leading to increased series resistance and hindered carrier extraction at low temperatures. Importantly, the thermal-cycling behavior presented in Fig. S3 shows that, despite their differing sensitivity to extreme cooling, all four devices maintain stable PCE over 16 thermal cycles between +20 °C and −85 °C. The negligible changes in V_{oc} and FF during cycling (Fig. S3) further indicate that no progressive thermal-fatigue-related degradation accumulates during repeated temperature swings [70]. Together, these findings demonstrate that while the NBG sub-device is the primary weak layer under deep-cold operation, the tandem architecture effectively mitigates resistive losses and

provides superior overall thermal robustness for aerospace environments. However, these results should be regarded as evidence of preliminary thermal-cycling resilience rather than a complete validation of long-term space durability, since 16 cycles is far below the number of thermal cycles expected during extended LEO operation and also below the more rigorous thermal-cycling requirements commonly used in terrestrial PV qualification standards, such as the 500-cycle test in IEC 61215. Therefore, while the results indicate that the devices can tolerate short-term repeated thermal stress without obvious thermal-fatigue-related degradation, further long-duration thermal--cycling studies involving hundreds to thousands of cycles are still required to assess their practical reliability for space applications.

Similar temperature-driven behavior has also been reported by Li et al., who linked these trends directly to structural changes in the perovskite film [71]. Fig. 6h and i shows the temperature-dependent 1D grazing-incidence wide-angle X-ray scattering (GIWAXS) diffraction profiles during cooling and heating. During cooling, the (001) peak broadens and weakens as the temperature decreases from 25 °C to −150 °C, indicating increased lattice disorder. This is further supported by the integrated area of the (001) diffraction peak in Fig. S4, which decreases at low temperature, reflecting reduced crystallinity, and recovers near room temperature, indicating that the absorber structure is largely restored. Thus, the lattice disorder changes dynamically with cyclic temperature rather than representing permanent degradation. This structural response agrees with device behavior: cooling to −160 °C causes a 27.9% PCE loss, mainly from FF reduction and increased hysteresis near the cubic-to-tetragonal transition around −50 °C, while J_{sc} remains nearly unchanged. During reheating, the recovery of the (001) peak and PCE confirms that the temperature-induced disorder is largely reversible. Li et al. further showed that this recovery is associated with lattice-strain relaxation, with nearly reversible out-of-plane behavior and only partial in-plane hysteresis/residual strain [71]. Overall, these results show that the perovskite absorber is thermally sensitive, but its structural quality can be mostly restored after returning to room temperature.

In contrast to the PSCs, organic solar cells are primarily affected by temperature variations through changes in charge transport and environmental conditions, rather than immediate intrinsic degradation of the active layer. Experimental observations under near-space conditions indicate that device performance is sensitive to temperature fluctuations, with trends consistent with thermally activated transport, in which current increases with temperature due to enhanced carrier mobility. At the same time, prolonged exposure to elevated temperatures is known to induce morphological changes in the photoactive layer, which can affect long-term performance. Under low-temperature conditions, device functionality can be maintained, although thermal management becomes critical due to the absence of convective heat transfer in low-pressure environments. Overall, these findings indicate that thermal effects in organic solar cells are governed by transport-related changes and environmental coupling, with stability largely dependent on operating conditions rather than rapid intrinsic material degradation [76].

3.5. UV

Following the discussion of thermal stress, it is also essential to evaluate how UV irradiation affects TSC stability, since the front-side transport and optical layers of perovskite top cells are known to interact strongly with short-wavelength light in space-relevant environments. In the perovskite/SHJ TSC reported by Zheng et al., UV exposure primarily reveals the weakness of the front transport/optical stack of the perovskite top cell, rather than the absorber junctions [81]. The authors point out that the “sun-facing” carrier-transport layer, in particular the spiro-OMeTAD HTL, introduces strong parasitic absorption in the near-UV (<420 nm), which wastes photons and limits the tandem's current output when the perovskite is used as a WBG top cell. During UV aging at 300-400 nm and 5 mW cm^{-2} (8 h per day for 36 days in N_2), the uncoated “baseline” TSC (no antireflection layer) and the device bearing only a textured polydimethylsiloxane (PDMS) antireflection (AR) coating without phosphor (DS0) each show about 10% PCE loss after 8 and 14 days, respectively; analysis of the parameter evolution indicates that this degradation is dominated by a fall in fill factor, followed by some J_{SC} loss, while V_{OC} remains “incredibly UV stable.” This behavior is consistent with UV-sensitive transport and interfacial regions at the sun-facing side, rather than a severe deterioration of the perovskite or Si junctions. To address this, Zheng et al. employ a family of textured PDMS AR films incorporating different loadings of $(Ba, Sr)_2SiO_4:Eu^{2+}$ phosphor, denoted DS0 (0 wt%), DS0.5 (0.5 wt%) and DS1 (1.0 wt%), which serve simultaneously as an AR coating, a light-trapping structure for the Si bottom cell, and a down-shifting layer that converts UV photons into green emission (around 517 nm) that is efficiently absorbed by the perovskite while circumventing parasitic absorption in spiro-OMeTAD. With the optimized DS0.5 coating, the 4 cm^2 TSC PCE increases from 20.1% (baseline, no AR; $J_{SC} = 14.1$ mA/cm^2, $V_{oc} = 1.73$ V, FF = 82%) to 23.1% ($J_{SC} = 16.5$ mA/cm^2, $V_{oc} = 1.73$ V, FF = 81%; 23.0% steady-state), and DS0.5 and DS1 devices retain 90% of their initial PCE after 27 and 36 days of UV stress, respectively, as shown in Fig. 7a, confirming that the sun-facing transport/optical stack is the most UV-susceptible region and that a phosphor-integrated PDMS AR layer is an effective mitigation approach [81].

Lee et al. engineered a textured antireflection coating (ARC) based on polydimethylsiloxane (PDMS) that is laminated on a monolithic perovskite/Si TSC [82]. The top perovskite cell uses a poly[bis (4-phenyl)(2,4,6-trimethylphenyl)amine] (PTAA)/mixed perovskite/[6,6]-phenyl-C_{61}-butyric acid methyl ester ($PC_{61}BM$)/zinc oxide (ZnO)/indium zinc oxide (IZO) stack, while the bottom device is a p-type Si cell with an aluminum back-surface-field contact, so that visible light is mainly absorbed in the perovskite and near-infrared light in Si. To manage UV and visible light, the PDMS ARC is loaded with silicate green aluminate (SGA) phosphor particles, which convert UV photons in roughly the 280–430 nm range into green emission around 530 nm, and with ~100 nm silicon dioxide (SiO_2) nanoparticles (NPs), which provide forward scattering and enhance diffuse transmittance. The combination suppresses reflection losses and compensates the backward scattering introduced by the large, high-index SGA particles, as quantified by the finite-difference time-domain (FDTD) scattering analysis in Fig. 7b. Device measurements in Fig. 7c show that, compared with a TSC without ARC or with simpler ARC variants, the optimized PDMS/SiO_2/SGA film, denoted ARC_S(0.8)SGA(0.8), meaning a PDMS ARC containing 0.8 wt% SiO_2 nanoparticles (“S”) and 0.8 wt% SGA phosphor particles, increases the J_{sc} to ≈16.7 mA/cm^2 and yields a PCE of 23.50% with a V_{oc} of 1.75 V and fill factor (FF) of about 80%. Although the TSC itself is not subjected to extended UV-aging in this work, the authors emphasize that parasitic UV absorption in transparent electrodes and buffer layers can both waste photons and accelerate perovskite decomposition, and they show on a single-junction Au/Spiro-OMeTAD/perovskite/TiO_2/fluorine-doped tin oxide (FTO) device that the ARC with phosphors maintains ~91% of its initial PCE after 120 h under 365 nm irradiation, illustrating that the same UV down-conversion principle can also mitigate UV-driven degradation [82]. Together, these studies illustrate that UV vulnerability in perovskite-based TSCs originates predominantly from the sun-facing transport and optical stack, and that front-side optical engineering, whether through down-shifting phosphors or combined scattering layers, offers an effective route to both enhance light harvesting and suppress UV-induced degradation.

However, when antireflection and down-shifting layers are considered for space applications, their optical benefit alone is not sufficient; their stability under UV/VUV radiation, vacuum, thermal cycling, charged particles, and atomic oxygen must also be verified. Although direct space-environment testing of the PDMS/phosphor AR layers discussed above remains limited, related NASA studies on space solar-cell

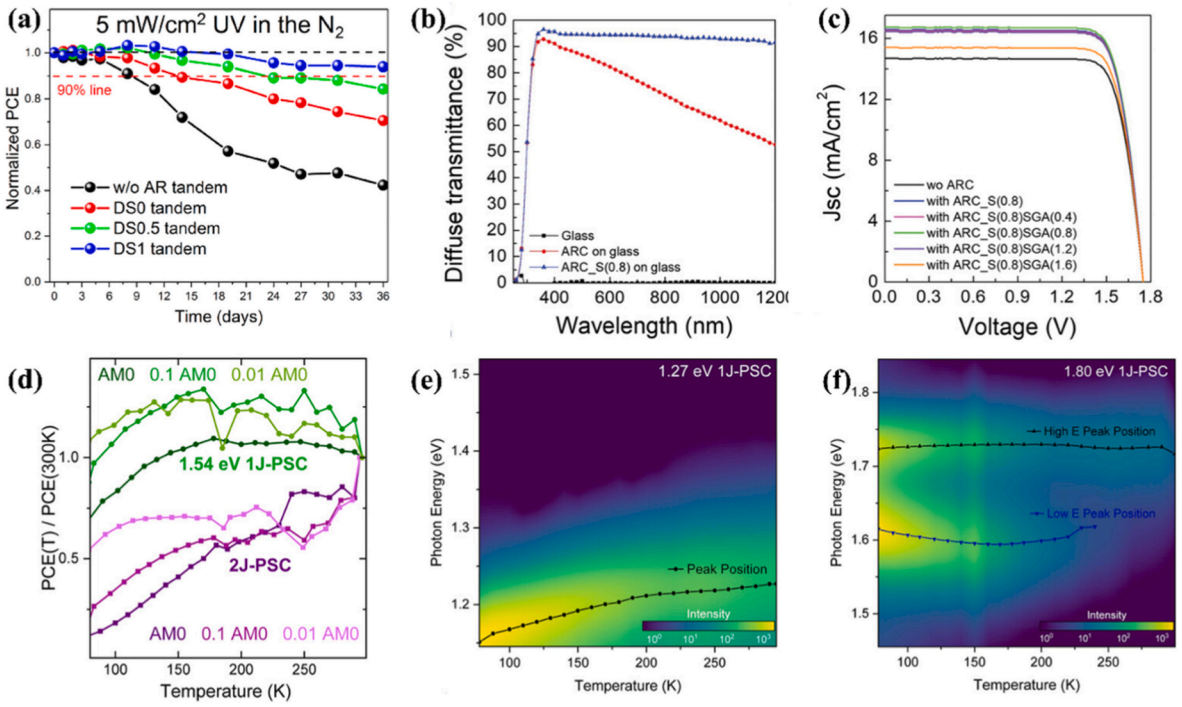

Fig. 7. Antireflection coatings and LILT response in perovskite tandem solar cells. (a) PCE evolution of the baseline tandem without ARC and perovskite/Si TSC incorporating DS0, DS0.5, and DS1 textured AR films during UV irradiation (5 mW cm^{-2}) under N_2 atmosphere [81]. (b) Diffuse transmittance spectra of bare glass, glass with a textured ARC film, and glass with a textured ARC_S (0.8) layer. (c) Current–voltage (J-V) characteristics of perovskite/Si TSCs employing different AR films [82]. (d) Normalized PCE, expressed as PCE(T)/PCE(300 K), of 1.54 eV single-junction (1J) and two-junction (2J) perovskite solar cells as a function of temperature under AM0, 0.1 a.m.0, and 0.01 a.m.0 illumination conditions. Temperature-dependent photoluminescence (PL) spectra of 1J perovskite solar cells under AM0 intensity, corresponding to emission energies of (e) 1.27 eV and (f) 1.80 eV, respectively [83].

cover systems have evaluated SiO_x, CeO_x, and TiO_x as antireflection coatings. These studies showed that TiO_x passed space-type coating qualification tests, including high temperature and abrasion tests, while providing higher AM0 output than conventional SiO_x-coated cells after cover glass integration. In contrast, CeO_x offered optical advantages but was mechanically unsuitable because of its soft/erasable nature, highlighting that AR coatings must satisfy both optical and environmental requirements. The associated evaporated glass-cover system was also examined under UV and 1 MeV electron irradiation, showing only limited degradation. Therefore, any AR layer proposed for space solar cells should be systematically evaluated under combined space-relevant stressors before being adopted in practical device designs [84].

3.6. LILT

Following the discussion of UV-exposure effects, the next critical space stressor is LILT operation, which amplifies recombination losses and destabilizes the mixed-halide top absorber, ultimately disrupting current matching in all-perovskite TSCs. Ozen et al. studied the effects of LILT on all-perovskite TSCs. The monolithic all-perovskite tandem architecture in this study consists of a 1.80 eV mixed-halide WBG top subcell stacked above a 1.27 eV Sn-Pb NBG bottom sub-cell [83]. Between the two absorbers, the authors employed a multilayer interconnect composed of a fullerene ETL (C_{60}), followed by AZO, ALD-SnO_x, and ALD-InO_x. This interlayer enables efficient recombination and optical coupling, meaning that any temperature- or illumination-driven instability in either absorber will propagate directly into the tandem's current-voltage behavior. The stability of these devices was assessed across a temperature range from 300 K to 80 K and under three irradiance conditions: AM0, 0.1 AM0 and 0.01 AM0), chosen to represent near-Earth and deep-space environments.

Fig. 7d shows that the TSC experiences a substantial efficiency decline when both temperature and irradiance are reduced. Cooling from 300 K to 80 K results in an 89.3% relative drop under AM0, while the corresponding reduction at 0.1 a.m.0 reaches 82.6%. However, under 0.01 a.m.0, the PCE stabilized at ~51.6% of the initial PCE. These intensity-dependent losses arise from the unequal thermal robustness of the two absorbers. As illustrated in Fig. 7e, the 1.27 eV lead-tin bottom-cell analogue remains stable throughout the 300-80 K range, exhibiting only a smooth photoluminescence (PL) redshift associated with bandgap narrowing and showing no evidence of phase transformation. In contrast, Fig. 7f reveals that the 1.80 eV mixed-halide top absorber undergoes a pronounced transition below approximately 240 K, where a new low-energy PL band emerges, indicating the formation of iodide-rich domains through temperature-accelerated halide segregation. This segregation modifies the optical absorption profile and enhances non-radiative recombination, thereby suppressing the attainable V_{oc} and fill factor across all illumination levels. Because the two sub-cells operate in series, the segregation-driven instability in the top sub-cell disrupts current matching with the bottom sub-cell, and these effects intensify under 0.1 a.m.0 and 0.01 a.m.0, where reduced photogeneration further limits charge extraction. Taken together, the trends captured in Fig. 7(d–f) identify the 1.80 eV mixed-halide top absorber as the principal origin of performance degradation under space-relevant LILT conditions [83].

In contrast to perovskite-based TSCs, where LILT conditions induce phase instability and current mismatch, organic solar cells are primarily limited by charge transport under such conditions. At low temperatures, reduced thermally activated hopping hinders carrier mobility and extraction, while lower illumination further suppresses photogeneration and enhances recombination losses. Organic devices are known to remain operational across a wide temperature range, with performance governed by temperature-dependent transport and illumination variations rather than abrupt material transformations. Unlike mixed-halide perovskites, no temperature-induced phase segregation was reported, indicating that LILT-induced degradation in organic solar cells is

dominated by transport limitations rather than intrinsic absorber instability [76].

4. Layer-by-layer vulnerability

Having discussed how space-relevant stressors affect TSC performance at the device scale, we now turn to a layer-by-layer analysis to identify the mechanisms that originate within the constituent materials themselves. This microscopic perspective allows the degradation pathways of each layer to be understood independently.

4.1. Top perovskite absorber

We begin with the perovskite top absorber, whose ionic composition, soft lattice, and exposure to the front-side environment make it the layer where the earliest and most consequential degradation processes originate. Three important degradation pathways observed in the top perovskite absorber are halide loss, ionization of shallow traps, and defect accumulation. Halide depletion emerges under both thermal and UV stress, but mixed-halide absorbers exhibit markedly different stability signatures. In the Br-doped perovskite (Fig. 8a), XPS shows iodine decreasing rapidly at 85 °C while bromine remains comparatively stable, leaving the film Br-rich and structurally intact for longer; UV aging reinforces this selectivity, producing PbI_2 within ~3 days and a Br-rich perovskite phase near 15°. By contrast, the Cl-doped system (Fig. 8b) loses N and Cl almost completely by ~21 days of heating, and iodine briefly becomes the dominant halide at day 7 before undergoing its own depletion. This behavior is consistent with the mixed halide reaction pathway described in equation (1), where the Cl-containing lattice releases volatile CH_3NH_3Cl and HCl while converting into an I-rich $MAPbI_3$ intermediate. The subsequent decline in iodine aligns with the progression outlined in equation (2), in which chloride-rich domains further decompose into volatile halides and $PbCl_2$. UV accelerates this pathway, with the absorber collapsing into $PbI_2/PbCl_2^-$ derived residues within only a few days. These contrasting trajectories demonstrate that Br incorporation suppresses halide volatilization, while Cl incorporation exacerbates it, defining a clear compositional hierarchy in top-absorber robustness [85].

$$CH_3NH_3PbI_{3-x}Cl_{x(s)} \rightarrow CH_3NH_3I_{(g)} + CH_3NH_{2(g)} + HI_{(g)} + HCl_{(g)} + CH_3NH_3Cl_{(g)} + CH_3NH_3PbI_{3(s)} + PbI_{2(s)} \quad (1)$$

$$CH_3NH_3PbCl_{3(s)} \rightarrow CH_3NH_3Cl_{(g)} + HCl_{(g)} + PbCl_{2(s)} \quad (2)$$

Shallow-trap ionization has emerged as a defining feature of recombination in triple-cation perovskite absorbers. Yuan et al. demonstrated that time-resolved PL measurements on these films produce decay transients spanning more than ten orders of magnitude, with differential decay times evolving from tens of nanoseconds to well above 100 μs [86]. As reported in Fig. 8c, the decay does not approach a single exponential but instead follows a power-law-like trajectory, reflecting a recombination regime dominated by repeated trapping and thermal release of carriers from shallow defect states. Their modeling analysis identifies at least three shallow traps located ~55, 95, and 125 meV from the nearest band edges, which ionize and detrap across the full transient. They further showed that the quadratic dependence of the initial PL amplitude on excitation density indicates that the films remain essentially intrinsic, so these traps act as dynamic charge reservoirs rather than dopants. To capture both the fast and slow portions of the decay, Yuan et al. combined time-correlated single-photon counting with gated-CCD detection, providing the required dynamic range to

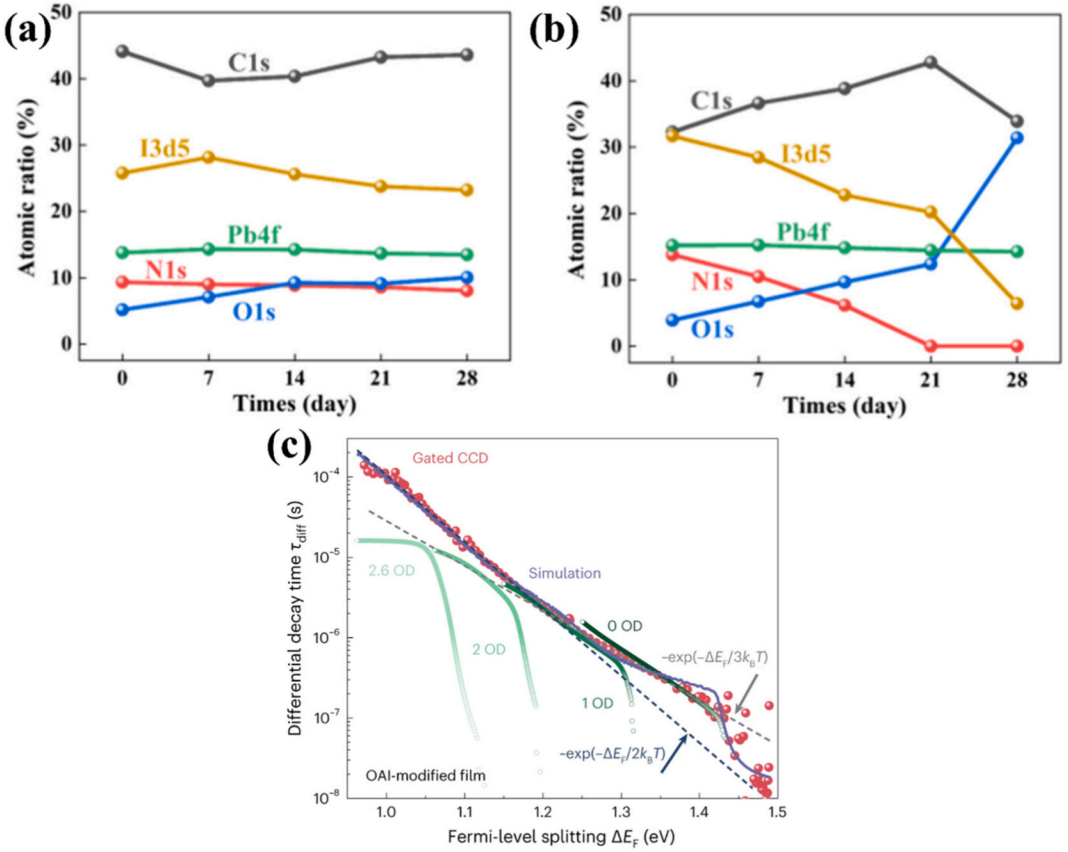

Fig. 8. Evolution of elemental composition during thermal degradation of (a)$MAPbI_{3-x}Br_x$ and (b) $MAPbI_{3-x}Cl_x$ perovskite films, determined by XPS [85]. (c) Differential PL decay time as a function of quasi-Fermi-level splitting, measured using time-correlated single-photon counting with different optical density (OD) filters and a gated CCD setup; the OD dataset closely overlaps with the gated CCD result, and the solid line represents the simulated trend [86].

resolve τ_{diff} as a function of quasi-Fermi-level splitting. Importantly, they observed the same long-tailed behavior in layer stacks and complete devices, indicating that shallow-trap ionization persists even in realistic architectures. These findings highlight that assigning a single lifetime to such absorbers is inappropriate, and that recombination must instead be described using effective, density-dependent coefficients [86].

Beyond chemical halide loss and trap ionization, irradiation also triggers structural-level changes, most notably the accumulation of point defects that reshape the internal electronic landscape of the perovskite layer. In proton-irradiated PSCs, the key degradation mechanism arises from iodine-vacancy defect accumulation in the perovskite absorber. Once vacancy densities grow into the 10^{16}-10^{-17} cm^{-3} range, these defects act as shallow donors and mobile ions, increasing trap density and drifting toward interfaces under bias. Their interfacial buildup reshapes internal fields, producing a rise in dark current, enhanced hysteresis, and delayed photocurrent response. The fact that oxygen exposure reverses these signatures highlights that the process is governed by mobile-defect accumulation, not irreversible perovskite decomposition [87].

4.2. ICL

The ICL is critical for enabling seamless carrier transfer between tandem sub-cells, and its buried position makes it highly sensitive to space-relevant stressors. The ICL must simultaneously act as an electrical recombination contact, optical window, chemical barrier, and mechanically compatible interface between the two sub-cells. In a 2T tandem, all photogenerated current must pass through this region; therefore, small changes in its conductivity, band alignment, defect density, or interfacial chemistry can strongly increase series resistance, disturb carrier recombination, and produce fill-factor loss or S-shaped J-V behavior. As schematically shown in Fig. 9, ICL degradation under space-relevant stressors can proceed through coupled radiation-induced, chemical, electrical, mechanical, and optical pathways. Because the ICL/recombination junction is the region where carriers extracted from the two sub-cells must recombine efficiently, any increase in contact resistance or recombination loss at this buried junction can limit the entire series-connected device. Radiation studies on perovskite tandem photovoltaics show that proton exposure can increase non-radiative recombination in buried recombination/contact regions, demonstrating that radiation damage is not limited to the absorber alone [62]. At the same time, the ICL must remain transparent to photons reaching the rear sub-cell and must survive subsequent layer deposition without sputter, solvent, or thermal damage. Under space-relevant stressors such as UV irradiation, thermal cycling, vacuum, and high-energy radiation, these coupled electrical, optical, and chemical requirements make the ICL one of the most vulnerable regions in monolithic TSCs [20].

In monolithic all-perovskite TSCs, the ICL must act not only as a recombination contact but also as a barrier against ionic and chemical cross-contamination between sub-cells. Mobile halide ions and metal species can diffuse through defective interlayers, causing interfacial reactions, recombination losses, and irreversible degradation. Ion migration and metal/halide interdiffusion can modify the local chemistry and electronic structure of the ICL. For example, C_{60}/SnO_{2-x} interconnection layers have been shown to form low-resistance Ohmic contacts with both wide- and narrow-bandgap perovskite sub-cells, indicating that the electronic behavior of the ICL strongly depends on interfacial composition and carrier transport across the buried contact [88]. If this interfacial composition or band alignment is altered by ion migration, radiation-induced defects, or interfacial reactions, transport or tunneling barriers can form at the recombination contact. These barriers restrict carrier recombination/extraction between the two sub-cells, increasing series resistance, reducing FF and voltage output, and producing S-shaped J-V behavior. In this context, ultrathin metallic recombination layers, such as Ag/MoO_x or Cu/Au, have been used in all-perovskite TSCs to improve recombination/contact transport and reduce resistive or S-shaped losses [89,90]. Therefore, dense and conformal ICL designs are important to suppress halide/metal interdiffusion while maintaining electrical and optical functionality. Under space-relevant stressors such as UV exposure, thermal cycling, vacuum, and energetic radiation, damage to the ICL could create defects or pinholes that accelerate ion migration. Thus, robust ICLs for space-compatible tandem PSCs should combine conductivity, transparency, chemical stability, and diffusion-barrier capability. ICL stability can be improved using dense conformal diffusion-barrier layers, chemically stable contact materials, ion-migration-resistant perovskite compositions, and robust encapsulation. Together, these strategies help

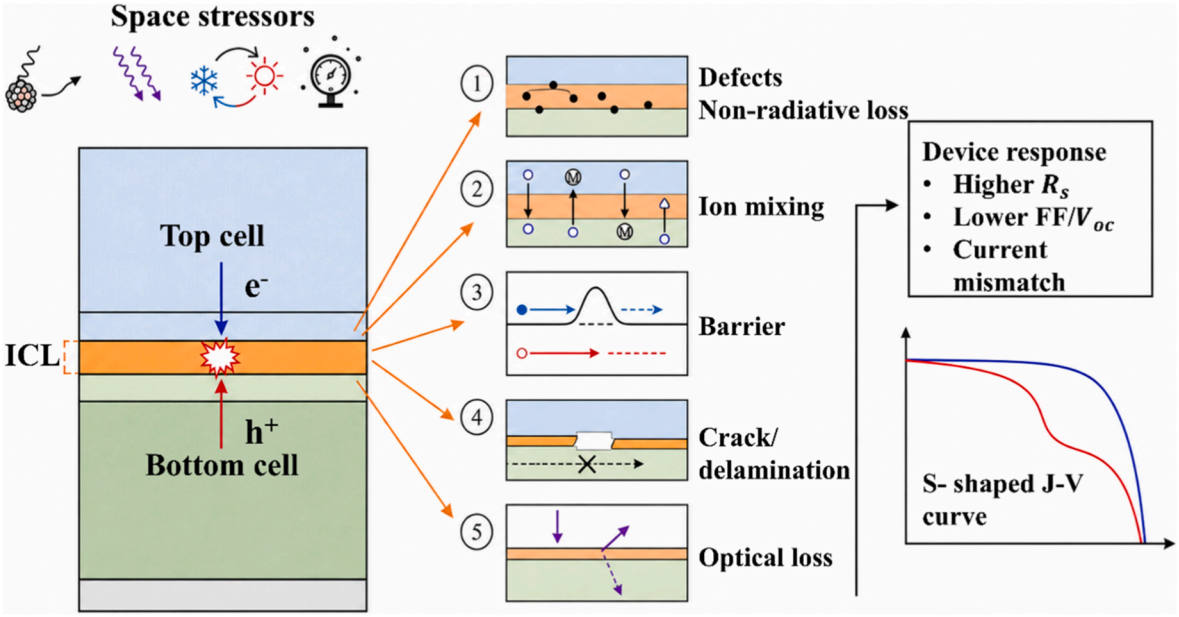

Fig. 9. Schematic illustration of coupled ICL/recombination-junction failure pathways in 2T perovskite tandem solar cells under space-relevant stressors. Radiation damage, ion/metal/halide interdiffusion, transport or tunneling-barrier formation, mechanical delamination, and optical losses can collectively increase series resistance, alter recombination, reduce rear-cell photocurrent, aggravate current mismatch, and produce S-shaped J-V behavior.

preserve carrier recombination, suppress halide/metal interdiffusion, and reduce stress-induced interfacial degradation [91].

As summarized in Table 1, existing data come mainly from proton-irradiation studies and an outdoor/thermal-cycling condition. Proton-irradiation studies on full perovskite/Si and perovskite/CIGS TSCs show that ICL regions are vulnerable, with MeV protons generating defects either within the junction itself or in the adjacent bottom sub-cell, ultimately increasing recombination in these buried interfaces. In contrast, standalone TCO layers, commonly used as recombination contacts in TSCs, exhibit far more benign responses under the proton stress, with ITO remaining largely unaffected and AZO showing only modest defect- and surface-chemistry changes. However, the optical role of the ICL remains critical because transparent conductive oxides and highly doped interlayers can introduce parasitic absorption, free-carrier absorption, or reflection losses, especially in the near-infrared region absorbed by the rear sub-cell [94]. Therefore, degradation or poor optical design of transparent conductive/oxide interlayers can reduce rear-cell photocurrent and aggravate current mismatch in 2T tandems. Beyond radiation, different vulnerabilities emerge from specific interlayer designs; for instance, the C_{60}/SnO_2 interface can undergo mechanically driven delamination under terrestrial outdoor and thermal-cycling conditions, indicating a structural rather than electronic failure mode. Mechanical delamination or cracking at the ICL/transport-layer interface can locally interrupt electrical contact, creating high-resistance regions and non-uniform current flow. Thermal-cycling studies of perovskite devices show that delamination at C_{60}/SnO_2-related interfaces can correlate with dark electroluminescence regions and strong current loss, supporting the role of mechanical contact failure in device degradation [93]. Since these tests are performed on Earth, where thermal cycling is generally milder than that expected in space, it is reasonable to expect that similar interlayers could experience even more severe thermomechanical stress and delamination risk under space-grade thermal cycling. Together, these mechanisms illustrate that while some ICLs are prone to radiation-induced recombination losses, others degrade primarily through transport, chemical, or mechanical instabilities, and systematic studies across broader space conditions are still lacking.

4.3. Bottom NBG perovskite sub-cell

The Sn-Pb narrow-bandgap bottom sub-cell is essential for near-infrared absorption and current matching in all-perovskite tandem solar cells. However, its Sn^{2+}-based chemistry introduces a strong oxidation pathway, making this layer a critical weak point under space-relevant stability conditions. The Sn-Pb narrow-bandgap bottom sub-cell is one of the most chemically vulnerable layers in all-perovskite TSCs because Sn^{2+} can oxidize to Sn^{4+}, causing self-p-doping, defect formation, and degraded charge transport. Leijtens et al. showed that partial Pb substitution slows Sn-based perovskite oxidation by altering the degradation pathway: pure Sn perovskites form SnO_2 and SnI_4, whereas mixed Sn-Pb compositions follow a modified pathway involving SnO_2, PbI_2, and I_2 [95]. Thus, Pb improves oxidation resistance but does not fully eliminate Sn^{2+} instability. Park et al. further confirmed this vulnerability in $FAPb_{0.5}Sn_{0.5}I_3$ films, where the Sn^{4+} fraction increased from 32.65% to 68.86% in the undoped film, while Ag doping limited the increase from 29.26% to 53.47%. This susceptibility of oxidation was also reflected in device stability: without encapsulation, the undoped Sn-Pb device retained only 6% of its initial PCE after 500 h, compared with 38% for the Ag-doped device (Fig. 10a). Cover-glass/paraffin encapsulation further improved stability, with the

Table 1
Comparison of ICL/recombination junctions and related contact layers in perovskite-based TSCs and single-junction devices, showing their dominant degradation mechanisms and quantitative performance changes under proton irradiation or operational stress.

Device Type	ICL/Recombination Junction	Stressor	Dominant Degradation Mechanism	Quantitative Impact/Observation	Reference
Perovskite/Si	SHJ (a-Si:H/TCO stack)	68 MeV protons, efficiency collapse already by $F \approx 1 \times 10^{11}$ p/cm^2 (max dose tested: 2×10^{12} p/cm^2)	Proton-induced defect generation in the Si heterojunction and bulk c-Si, creating strong recombination centers that quench J_{sc} and EQE of the silicon sub-cell.	Under AM0, perovskite/SHJ TSC power falls from ≈257 W/m^2 to ≈4 W/m^2 (≈1–2% of initial),	62
Perovskite/CIGS	ALD NiO-based recombination contact (ZnO/NiO/PTAA)	68 MeV protons, $F = 2 \times 10^{12}$ p/cm^2	Proton-induced trap states in the CIGS bottom cell (≈60% of loss) plus increased interfacial recombination in the NiO-based recombination contact (≈40% of loss); perovskite bulk remains largely unaffected.	Retains >85% of initial efficiency; far more radiation-hard than the perovskite/SHJ TSC.	62
Standalone ITO	TCO thin film; proxy for recombination TCO in P/Si and P/CIGS TSCs	226.5 MeV protons, fluence 10^{11} p/cm^2	Minimal impact of high-energy protons; XRD, SEM, ellipsometry and XPS show essentially unchanged structure and surface chemistry. Optical constants and transmission are unchanged within error; sheet resistance increases only ≈1.8%.	T(λ) (spectral transmittance at wavelength λ) stays >80% after irradiation; R_s (sheet resistance in Ω/□) shifts only slightly (≈9.1 → 9.27). No structural change in XRD.	92
Standalone AZO	TCO thin film; proxy for recombination TCO	226.5 MeV protons, fluence 10^{11} p/cm^2	Proton irradiation introduces additional defects and modifies surface chemistry (increased AlO_x, shifted XPS peaks), making AZO more affected than ITO. Transmittance in 400–630 nm decreases, and ellipsometry shows an increased extinction coefficient at λ > 1000 nm consistent with increased free-carrier absorption.	T(λ) remains >80% but decreases in the visible; R_s drops from ≈302 → ≈202 Ω/□ (≈33%), indicating increased conductivity.	92
Single-junction inverted PSC	C_{60}/SnO_2 electron-transport stack	Outdoor operation (Israel, Cyprus, Germany) + indoor thermal cycling (−40 ↔ 85 °C, ISOS-T-3)	Encapsulant-induced partial delamination with the crack initiating at the C_{60}/SnO_2 interface (mechanically weakest region). Delamination locally interrupts contact between ETLs and perovskite, creating very high series resistance and blocking charge extraction.	In delaminated cells, loss of active area (dark electroluminescence (EL) regions) correlates with a strong drop in J_{sc}; non-delaminated cells show no J_{sc} loss. Delamination appears within weeks in hot climates (Israel, Cyprus) but not over 1-2.5 years in Germany.	93

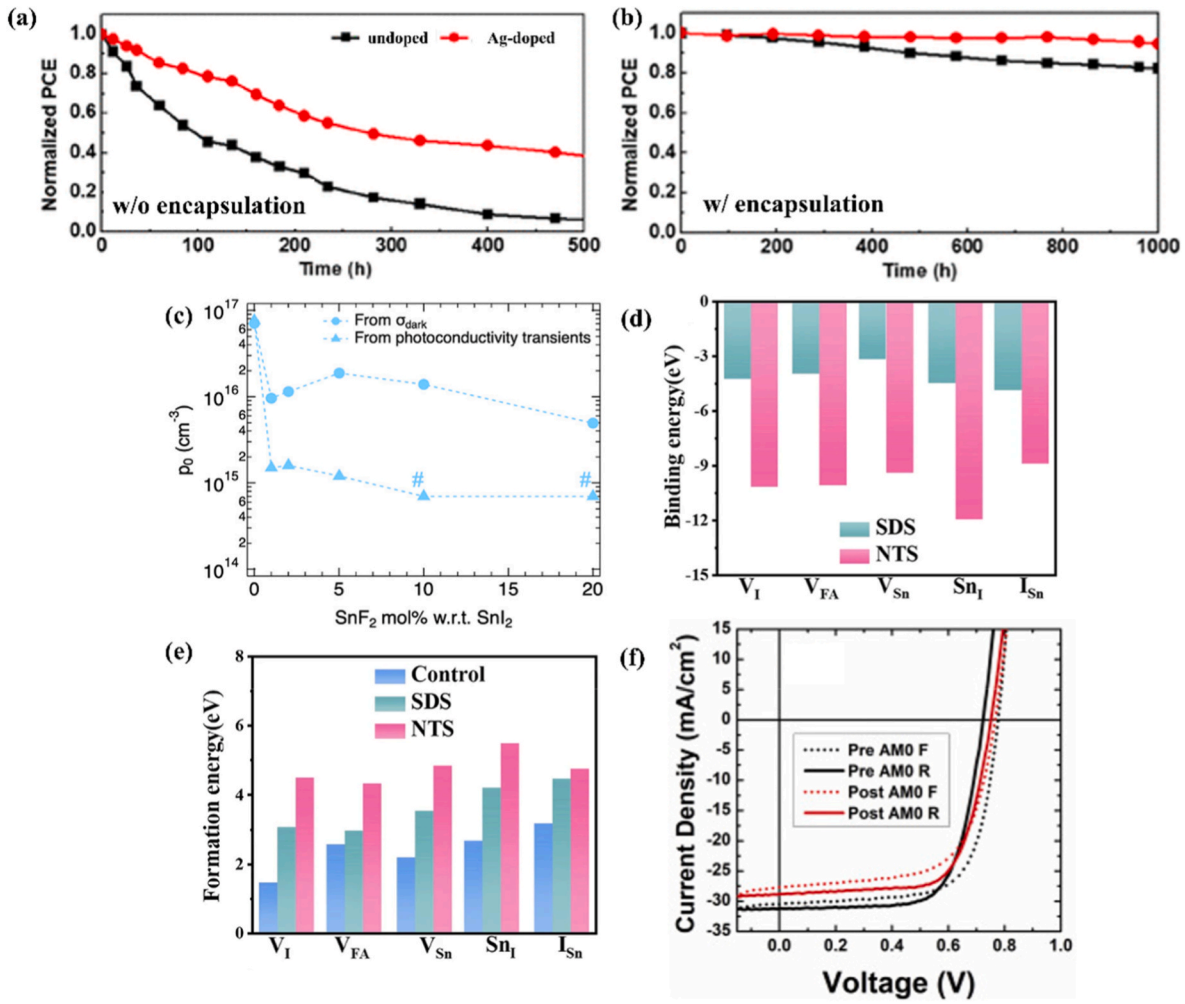

Fig. 10. Stability and defect-related properties of Sn-Pb PSCs relevant to tandem device reliability. (a,b) Normalized PCE as a function of storage time for PSCs without and with encapsulation, comparing devices without and with Ag doping [96]. (c) Variation of the hole density parameter, p_o, as a function of SnF_2 concentration [97]. (d,e) Calculated binding energies (E_β) of SDS and NTS with Sn, FA, and I vacancy defects (V_{Sn}, V_{FA}, and V_I), iodine interstitial defects (I_i), and iodine substitution at the Sn site (I_{Sn}) on the perovskite surface, together with the corresponding defect formation energies (E_f) [98]. (f) J-V characteristics under 1-sun AM0 illumination before and after proton irradiation at a fluence of 1×10^{11} p/cm^2 [99].

Ag-doped device retaining 95% of its initial PCE after 1000 h compared with 82% for the undoped device (Fig. 10b) [96]. However, for space applications, such encapsulation should be considered preliminary until validated under combined stressors such as vacuum, UV irradiation, thermal cycling, atomic oxygen, and ionizing radiation. Overall, these studies show that although Pb alloying and dopant strategies suppress Sn oxidation, the Sn-Pb bottom sub-cell remains a critical degradation-sensitive layer in tandem architectures.

Self-p-doping is another key vulnerability of the Sn-Pb narrow-bandgap bottom sub-cell, because excess background holes accelerate nonradiative recombination and reduce carrier lifetime. Meggiolaro et al. explained this behavior from the defect-chemistry perspective, showing that Sn-based perovskites favor acceptor-type defects such as tin vacancies and interstitial iodine, which shift the material toward intrinsic p-type behavior [100]. In mixed Sn-Pb perovskites, Pb incorporation partially moderates this defect chemistry, but the presence of Sn still leaves the bottom absorber susceptible to self-doping and trap-assisted recombination. Nespoli et al. experimentally quantified this effect in $Cs_{0.25}FA_{0.75}Sn_{0.5}Pb_{0.5}I_3$ films, showing that Sn oxidation produces dark free holes in the perovskite layer [97]. As shown in Fig. 10c, SnF_2 addition markedly reduced the dark free-hole density, p_o, confirming that suppressing Sn^{4+} incorporation can lower self-doping in mixed Sn-Pb absorbers. However, because additive-based control may also introduce surface heterogeneity or SnO_x accumulation, self-doping mitigation must be evaluated together with long-term chemical and interfacial stability, especially under space-relevant stressors [97].

Defect formation is another important vulnerability of the Sn-Pb bottom sub-cell, since lattice strain, ion migration, and Sn-I bond instability can generate vacancies and antisites during operation. Xu et al. showed that defect behavior in mixed Pb-Sn perovskites is composition-dependent, with 30-70% Sn compositions showing improved defect tolerance and the 50% Sn composition giving longer carrier lifetimes than Sn-poor or Sn-rich films [101]. Bai et al. further showed that sodium naphthalene-1,3,6-trisulfonate (NTS) can stabilize the Sn-Pb lattice through coordination between its sulfonate groups and Sn^{2+} sites. The binding-energy plot shows that NTS binds more strongly than SDS to several intrinsic defect sites, while the defect-formation-energy plot shows higher formation energies for iodine vacancies, Sn vacancies, FA vacancies, and antisite defects after NTS treatment (Fig. 10d and e). This indicates that NTS not only passivates existing defect-prone sites but also makes new defect formation less favorable [98]. Overall, although Sn-Pb absorbers can be engineered toward improved defect tolerance, defect formation remains a key degradation pathway under prolonged operational stress.

Radiation resistance is an important requirement for the Sn-Pb bottom sub-cell in space-operating tandem solar cells because energetic

particles can induce lattice vacancies and carrier-collection losses. Durant et al. investigated mixed $(FASn)_{0.6}(MAPb)_{0.4}I_3$ PSCs under 3.7 MeV proton irradiation at a fluence of 1×10^{11} p/cm^2. The light J-V results showed that the device retained most of its PV response after irradiation, with only a small relative PCE loss of 4.6% (Fig. 10f). The degradation was mainly associated with reduced J_{sc} and a slight FF loss, while V_{oc} was largely retained. These findings indicate that Sn-Pb perovskites can exhibit strong proton tolerance [99].

Taken together, the Sn-Pb bottom sub-cell remains a key stability-limiting layer in all-perovskite TSCs because Sn oxidation, self-doping, defect formation, and radiation-induced carrier-collection losses can strongly affect device durability. Although alloying and additive strategies can partially suppress these pathways, detailed studies on vacuum sensitivity and space-compatible encapsulation remain limited. Therefore, Sn-Pb sub-cells and their encapsulation stacks must be directly tested under combined space-relevant stressors before they can be considered reliable for space operation.

4.4. Bottom Si/CIGS/organic solar cell

In a monolithic TSC, the bottom silicon junction often sets the end-of-life ceiling because displacement damage manifests primarily through two coupled mechanisms: the formation of Shockley-Read-Hall (SRH) recombination centers that reduce the bulk minority carrier lifetime, and dopant compensation that increases resistivity and series resistance. In this context, two silicon bottom-cell architectures are considered: passivated emitter and rear cell (PERC), which employs localized rear contacts through a dielectric passivation layer, and tunnel oxide passivated contact (TOPCon), which uses a full-area, carrier-selective poly-Si/ultrathin SiO_x rear contact to suppress recombination and reduce contact resistance. In a study by Ma et al., 1 MeV electron irradiation is modeled by introducing five deep defect levels (two donor-like and three acceptor-like), with capture cross sections ranging from relatively weak recombination centers (for example, 8.9×10^{-17} cm^2 at $E_v + 0.18$ eV and 1.8×10^{-16} cm^2 at $E_c - 0.18$ eV) to very strong SRH centers (about 6.3×10^{-13} cm^2 at $E_v + 0.56$ eV and 3.55×10^{-13} cm^2 at $E_c - 0.71$ eV) [102]. Because the defect density is assumed to decay only weakly through the wafer thickness, with an exponential depth factor of approximately 960 μm, the damage is effectively bulk-like over typical Si bottom-cell thicknesses. This physics is reflected at the device level in Fig. 11a and b, where both p-type PERC and p-type TOPCon bottom cells show a gradual, fluence-dependent reduction in normalized J_{sc}, V_{oc}, fill factor, and efficiency under 1 MeV electron irradiation; at the relatively high substrate doping used for that comparison, the normalized degradation trends are nearly identical, indicating that SRH recombination from radiation-induced defects dominates the response in both architectures. When the acceptor concentration is reduced, the degradation pathways diverge: while the reduction in V_{oc} remains similar for PERC and p-TOPCon, consistent with a common SRH-limited lifetime mechanism, the fill factor degrades much more strongly in PERC at low doping. This difference arises because radiation-induced majority-carrier removal increases the bulk resistivity, and the localized rear contacts in PERC amplify the associated series-resistance penalty through lateral carrier transport, whereas the full-area passivated rear contact in TOPCon mitigates this effect. Consequently, although both bottom-cell architectures are governed by the same fundamental radiation-induced defect physics, TOPCon retains a relative end-of-life advantage when the silicon bottom junction is optimized toward lower doping for higher beginning-of-life performance in TSCs [102].

By comparison, CIGS bottom cells respond to radiation primarily through the formation of irradiation-induced defect states within the chalcopyrite absorber, rather than through strong dopant compensation effects as in crystalline silicon. Proton or electron irradiation introduces vacancy-interstitial defect pairs and deep recombination centers associated with native Cu, In, and Ga defects, which increase non-radiative recombination and reduce V_{oc} and carrier lifetime. A key distinction is that a significant fraction of the radiation-induced degradation in CIGS can be partially reversed by post-irradiation heat–light soaking, indicating that mobile native defects can reorganize or annihilate under operating conditions. As a result, CIGS bottom cells often exhibit comparatively higher radiation tolerance and partial self-recovery, making them a resilient alternative to silicon for TSC architectures under space environments [103].

In organic solar cells, radiation-induced degradation follows a fundamentally different pathway compared to crystalline and chalcopyrite absorbers, arising from the soft-matter nature of the active layer. High-energy radiation primarily induces bond cleavage and radical formation within the conjugated organic network, which can trigger side reactions and alter the morphology and electronic structure of the photoactive layer. These changes lead to increased energetic disorder and enhanced non-radiative recombination, reflected at the device level by reductions in V_{oc} and fill factor rather than pronounced current loss. Notably, the impact of radiation can depend on the molecular structure, as systems with stronger conjugation exhibit reduced susceptibility to permanent defect formation and, in some cases, limited electronic degradation after irradiation. Furthermore, interface effects play a critical role, with electrode and contact engineering shown to mitigate voltage losses induced by charge accumulation. As a result, organic bottom cells exhibit a degradation pathway dominated by chemical and morphological perturbations rather than bulk defect physics, offering a distinct response to radiation within tandem architectures [76].

4.5. CTLs (HTL/ETL)

While degradation of the absorber and bottom sub-cell often sets the operational limits of the device in single-junction and tandem perovskite

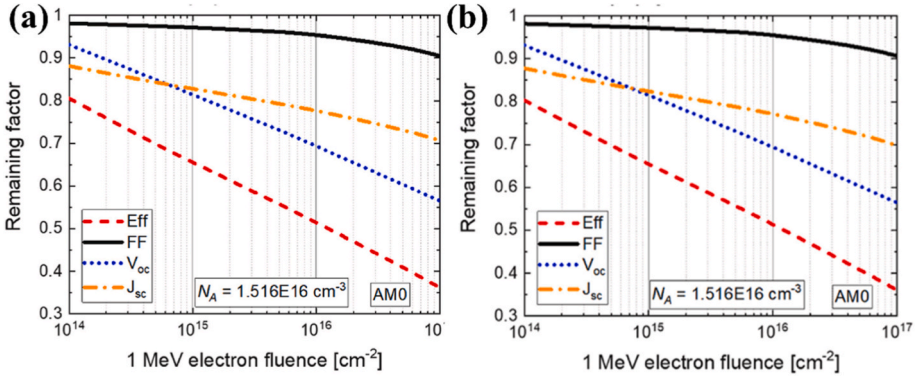

Fig. 11. Normalized performance parameters of crystalline silicon solar cells as a function of 1 MeV electron fluence for (a) PERC and (b) p-TOPCon architectures, with all values normalized to their beginning-of-life (BOL) performance [102].

photovoltaics under space-relevant conditions, these effects alone do not fully account for the diversity of observed device-level failure modes. Increasing evidence indicates that performance losses frequently originate in the surrounding functional layers that mediate charge extraction and injection. In this context, the literature summarized in Table 2 shows that results across single-junction perovskite solar cells, monolithic TSCs, and standalone charge-transport-layer studies consistently demonstrate that charge-transport layers (CTLs) play a decisive role in governing stability under space-relevant stressors. Under particle irradiation, device failure thresholds are strongly influenced by organic HTLs, where radiation-induced de-doping and transport loss can dominate high-fluence degradation, while inorganic ETLs such as SnO_2 primarily exhibit moderate resistivity increases without directly inducing catastrophic device failure. Ultraviolet stress further reveals a pronounced materials contrast, with TiO_2 ETLs accelerating photocatalytic interfacial degradation, whereas SnO_2 ETLs provide comparatively improved UV tolerance under identical conditions. Thermal and low-temperature studies decouple chemical stability from transport limitations, showing that inorganic HTLs (NiO_x) maintain structural and electrical robustness, while molecular ETLs (e.g., C_{60}) can limit tandem performance through transport bottlenecks at low temperature, even in the absence of chemical degradation. Collectively, these findings highlight that CTL reliability in space environments is highly stressor-dependent and dominated by interface chemistry and carrier-transport constraints rather than bulk absorber instability.

Self-assembled monolayers (SAMs) have become widely used HTLs in recent p-i-n PSCs and TSCs because they provide ultrathin, conformal, and low-parasitic-absorption contact layers. Phosphonic-acid-based carbazole SAMs such as 2PACz, MeO-2PACz, and Me-4PACz have been used to improve hole extraction and enable high-efficiency monolithic perovskite/Si TSCs [109–111]. For example, a study by Al-Ashouri et al. introduces conformal SAM contacts for perovskite single-junction and monolithic TSCs, while a later study used Me-4PACz to realize >29% efficient monolithic perovskite/Si TSCs [112,113]. Therefore, SAMs should be included among the key CTL/contact materials in TSCs. SAM-based HTLs have already been applied in high-efficiency monolithic perovskite/Si and all-perovskite TSCs, and some reports show promising stability under light soaking, damp heat, and thermal cycling. However, their stability under space-specific stressors, particularly vacuum, AO, energetic particle irradiation, vacuum-UV exposure, and LILT operation, remains insufficiently explored.

Interface passivation can also be considered an additional option to reduce CTL-related losses under space-relevant stress. In tandem architecture, passivating the CTL/perovskite contact can reduce interfacial trap density, suppress non-radiative recombination, improve energy-level alignment, and limit chemically driven degradation at buried interfaces. For example, Zhumagali et al. used an organometallic dye molecule to passivate the NiO_x/perovskite interface in textured monolithic TSCs, reducing surface traps and undesirable interfacial reactions [114]. Chin et al. demonstrated interface passivation for high-efficiency perovskite/Si TSCs, highlighting the importance of suppressing recombination at textured tandem interfaces [115]. More recently, Liu et al. reported bilayer interface passivation in perovskite/Si TSCs, combining improved electron extraction with reduced non-radiative recombination [116]. Therefore, alongside CTL-material selection, targeted interface passivation may help reduce stress-induced FF and V_{oc} losses in tandem stacks.

4.6. Encapsulation, electrodes and substrates

Beyond CTL degradation, device reliability is increasingly governed by the stability of encapsulation and electrodes, which control environmental isolation and contact integrity under space stressors. As summarized in Table 3, studies of AO exposure indicate that encapsulants and cover films may appear chemically stable initially, but mechanical changes often limit their long-term performance. For both silicon-based and polymer-based materials, AO exposure tends to modify the surface in a way that initially slows erosion but gradually alters stiffness and internal structure. In polymer cover films, this typically involves the loss of organic components and the formation of silica- or silicate-rich surface layers, which reduce erosion rates but do not fully block AO penetration, especially when AO acts together with UV radiation [117–119]. Table 3 also indicates that AO-related degradation is not limited to encapsulants but can also affect electrodes and TCOs. For metals, AO-induced oxidation may increase contact resistance, particularly for exposed Ag, while TCOs such as ITO may experience changes in surface oxygen stoichiometry that alter sheet resistance or work function. These effects are especially relevant in TSCs, where electrode/TCO layers often serve as recombination or interconnecting contacts.

Beyond these AO-related effects, encapsulation strategies for space-compatible TSCs should be distinguished from conventional terrestrial packaging. Terrestrial PV encapsulation is mainly designed to suppress moisture/oxygen ingress, maintain adhesion, and survive standard damp-heat or thermal-cycling qualification tests [128]. In contrast, space encapsulation must function as a multifunctional barrier under harsher environmental and design constraints. These include AO erosion in LEO, UV/VUV-driven degradation, radiation-induced darkening or contamination-related optical loss, vacuum-induced outgassing, CTE mismatch, low areal mass, and launch/deployment-related mechanical stress [67,129]. These requirements are especially important for 2T TSCs because the encapsulation or cover layer is not only a protective barrier, but also part of the optical path that controls photon delivery to the top and bottom sub-cells [128,130]. For example, a barrier layer that improves AO or radiation resistance may also introduce parasitic absorption, reflection, yellowing, or spectral filtering. This can reduce the top-cell photocurrent; because 2T tandems are series-connected, the resulting current imbalance limits the current of the entire device and reduces overall efficiency [130]. Similarly, a mechanically rigid barrier may improve environmental isolation but increase interfacial stress during thermal cycling or deployment [8]. Thus, space-compatible encapsulation should balance environmental protection, AM0 optical transparency, radiation and UV/VUV stability, thermomechanical compatibility, low mass, and minimal disruption to current matching. Quantitative material-selection metrics, including AO erosion yield, glass-transition temperature, CTE, and yellowing index, are discussed further in the next section.

Hyperthermal AO exposure further shows that silicone-based encapsulants can develop surface cracking. For space-grade CV-1144-0 silicone, AO exposure at room temperature produced clear cracks on the surface, as shown in Fig. 12a. This cracking is attributed to the formation of a silicon oxide layer during AO bombardment; because this layer is denser than the underlying silicone, shrinkage-induced stress leads to surface cracking. Although the oxide layer reduces erosion and provides partial protection, cracks can expose the underlying silicone and allow continued AO attack. Thus, the AO reliability of silicone encapsulants is governed not only by their low mass-loss rate but also by the mechanical integrity of the oxidized surface layer [131]. Overall, the results summarized in Table 3 indicate that the reliability of encapsulants in space is mainly controlled by stress buildup and contamination accumulation, rather than by chemical resistance alone.

As summarized in Table 3, substrate and cover-layer stability are also relevant to TSC reliability because these layers determine optical transmission and provide mechanical support for the device stack. Radiation-induced darkening in glass and degradation of polymer substrates under AO, UV exposure, and thermal cycling can reduce photon delivery, weaken adhesion, and compromise long-term structural integrity.

Beyond these effects, the thermal stability of metal contacts becomes a key limitation, as demonstrated by Domanski et al. [132]. In Fig. 12b, ToF-SIMS depth profiles show that Au remains confined near the electrode region in control and 30 °C-aged devices, whereas aging at 70 °C

Table 2
Reported degradation pathways of ETLs and HTLs, in PSCs and TSCs under space-relevant stressors (proton and gamma irradiation, UV exposure, thermal stress, vacuum, and low-temperature operation), highlighting the dominant physical or chemical mechanisms and their quantitative impact on device performance.

Layer Type	Material	Architecture	Space Stressor	Dominant Degradation Mechanism	Key Quantitative Result	Reference
HTL	Spiro-OMeTAD	Planar n-i-p perovskite solar cell (Cs/MA/FA mixed-cation absorber)	Proton (250 keV)	Proton-induced deterioration and de-doping of the spiro-OMeTAD HTL, identified as the primary cause of device degradation at high fluence	Device performance remains essentially unchanged up to 1×10^{13} p/cm^2, while complete electrical failure occurs at 6×10^{14} p/cm^2	104
ETL	SnO_2	Planar n-i-p perovskite solar cell (Cs/MA/FA mixed-cation absorber)	Proton (250 keV)	Radiation-induced defect formation in SnO_2/FTO substrates leading to increased resistivity; however, ETL degradation is not the primary cause of device failure	Square resistance of glass/FTO/SnO_2 substrates increases by ~16% at a fluence of 6×10^{14} p/cm^2, while recycled devices recover full photovoltaic performance	104
ETL	TiO_2 (mesoporous TiO_2 ETL in a normal n-i-p device)	n-i-p (FTO/bl-TiO_2/mp-TiO_2/perovskite/Spiro-OMeTAD/Au)	Strong UV exposure (365 nm) in an inert N_2 atmosphere (nitrogen-filled glovebox)	UV-driven TiO_2 photocatalysis at the TiO_2/perovskite interface (photogenerated holes oxidize $I^- \rightarrow I_2$; concurrent interfacial decomposition leading to pinholes/voids and separation)	PCE drops by ~50% after 110 min of UV exposure; cross-sectional SEM shows pinholes/voids and interfacial separation at the TiO_2/perovskite contact	43
ETL	SnO_2 (mesoporous SnO_2 ETL)	n-i-p (normal) perovskite solar cell with mp-SnO_2 ETL	Strong UV exposure (365 nm) in an inert N_2 atmosphere (nitrogen-filled glovebox)	UV-driven decomposition at the perovskite/mp-SnO_2 interface with formation of hole structures; interfacial separation limits carrier injection (degradation is slower than for mp-TiO_2).	PCE decreases by ~10% after 110 min UV exposure (mp-SnO_2 shows significantly better UV stability than mp-TiO_2 under the same conditions)	43
HTL	PTAA	p-i-n (ITO/PTAA/$FA_{0.9}Cs_{0.1}PbI_3$/C_{60}/BCP/Cu)	UV-containing illumination (unfiltered sunlight/LEP lamp with UV component)	UV accelerates degradation at the buried ITO/PTAA/perovskite interface (weak interfacial bonding → increased interfacial trap density → accelerated A-site cation migration/phase segregation near the bottom interface), rather than PTAA bulk polymer degradation being the main driver	UV-irradiated PTAA shows an absorption peak decrease of ~45%, yet devices made using UV-irradiated PTAA lose only ~0.5% PCE; under UV-containing LEP exposure, device trap density increases with time.	105
HTL	NiO_x (rf-sputtered, polycrystalline)	p–i–n (ITO/NiO_x/perovskite ($MAPbI_{3-x}Cl_x$)/$PC_{61}BM$/AZO/Ag)	Thermal stress at 85 °C (accelerated aging under 1-sun + MPPT; also tested in dark at 85 °C)	Thermal-only degradation is negligible (no PCE loss in dark at 85 °C for >1000 h); under illumination + maximum power point tracking (MPPT), performance loss occurs but is significantly mitigated by the sputtered NiO_x HTL compared with PEDOT:PSS-based devices	Retains ~73% of initial efficiency after 1000 h at 85 °C under 1-sun + MPPT; encapsulated devices show no degradation after >1000 h storage at 85 °C in dark (PEDOT:PSS devices retain <20% after 400 h at 30 °C under operation)	106
ETL	C_{60}	Monolithic all-perovskite TSC (2J)	LILT; 300 → 80 K	Low-temperature transport limitation: reduced hopping conductivity in C_{60} increases series resistance and causes FF collapse (transport physics, not chemical degradation)	Severe FF loss and up to ~89% relative PCE reduction at low temperature; TSC performance limited by transport bottleneck under LILT.	83
HTL	PEDOT:PSS	Thin-film (spin-coated on Si/SiO_2; standalone HTL material study)	Gamma-ray (^{60}Co), irradiated in air vs vacuum, total dose up to 3 kGy	Ionizing-radiation–induced defects drive chain scission and/or cross-linking, reducing charge delocalization (bipolaron →polaron evolution) and lowering mobility/conductivity; irradiation environment modulates carrier concentration (vacuum > air)Up to 3 kGy: no significant Raman-identified conformational change, but conductivity and mobility drop with dose; Hall shows higher carrier concentration in vacuum than air (mobility decreases in both)	Up to 3 kGy: no significant Raman-identified conformational change, but conductivity and mobility drop with dose; Hall shows higher carrier concentration in vacuum than air (mobility decreases in both)	107
Absorber/Perovskite-HTL interface	MAFA perovskite $(MAPbBr_3)_{0.17}(FAPbI_3)_{0.83}$/Spiro-OMeTAD	n-i-p (ITO/SnO_2/MAFA/Spiro-OMeTAD/Au)	Vacuum + illumination	Vacuum operation under light induces pronounced lattice shrinkage and light-driven phase segregation in MAFA; under electrical bias, excess PbI_2 migrates toward the perovskite/Spiro-OMeTAD interface, contributing to V_{OC} degradation	100) Bragg peak shifts from 0.998 to 1.018 Å^{-1} within 45 min of illumination in vacuum, evidencing rapid lattice contraction and phase instability	72
HTL	NiO_x (ALD-deposited)	p-i-n (inverted perovskite solar cell)	Chemical interaction during perovskite deposition (interfacial chemistry)	Hydroxyl-rich ALD-NiO_x surface chemically interacts with perovskite precursors, leading to interfacial defect formation, non-ideal crystallization, and enhanced interfacial recombination	XPS reveals a high density of surface –OH species on ALD-NiO_x; devices exhibit increased interfacial recombination and degraded V_{oc}/ *FF* unless the NiO_x surface is chemically or thermally treated	108

Table 3
Effects of space stressors on commonly used protective/encapsulation materials and substrates, summarizing their typical applications and the dominant erosion, oxidation, or synergistic AO–UV, radiation degradation mechanisms reported.

Stressors	Material used	Common usage of the material	Failure mode and mechanism	Reference
AO (Simulated LEO), 2 h	SiO (1 μ m) on PSCs	Thin-film barrier/ protective coating	No degradation observed for SiO-encapsulated cells; except a small EL decrease for PEAI-passivated cells after 60 min, possibly due to gradual SiO erosion by AO	[78]
AO (Ground Simulation)	6FCDA-Polyimide Films	Cover film	AO-driven surface erosion from preferential carbon volatilization, accompanied by in-situ formation of a protective SiO_x/silicate layer that slows further recession.	[117]
AO + UV Synergy	MIL-53(Al) on PI	Research coating for AO + UV protection	UV-induced breathing and particle refinement increase boundary density and mesopores, providing pathways for AO penetration while partially dissipating AO kinetic energy.	[118]
LEO AO exposure (in-space: LDEF 5.8 years; Mir >10 years; EOIM-III Shuttle exposure)	Silicone materials (coatings)	Sealants/encapsulation compounds	AO oxidizes silicone to silica, stiffening the surface and inducing tensile stress that leads to cracking and loss of protective function; AO also fixes silicone contamination into silica deposits that accumulate and, under AO + UV, darken and degrade optical performance.	[119]
AO/LEO exposure	Ag	Metal electrode	AO can oxidize Ag and form silver oxide products. Because Ag shows poor AO compatibility, exposed Ag contacts may suffer optical/electrical degradation and should be protected by barrier layers.	[120]
AO/LEO exposure	Metals such as Al, Au, Ag	Metal electrode	AO-induced oxidation affects metals differently: Al forms a more protective oxide, Au is comparatively resistant, whereas Ag reacts more rapidly. Therefore, metal electrode stability under AO depends strongly on oxide adherence and electrical/contact resistance changes.	[121]
LEO AO	ITO	TCO	ITO generally shows very low AO erosion, but LEO exposure can still alter electrical properties; oxygen-rich surface modification can change oxygen-vacancy concentration, carrier density, work function, and contact resistance. Such changes may disturb energy-level alignment in TCO-based ICLs	[122]
Gamma irradiation	Glass	Substrate	Cerium doping suppresses radiation-induced darkening and improves optical transmission stability under electron irradiation.	[123]
Electron irradiation	Cerium-doped cover glass	Radiation resistant cover glass	Cerium doping suppresses radiation-induced darkening and improves optical transmission stability under electron irradiation.	[124]
AO	PI	Flexible substrate	AO causes surface erosion, roughening, and mass loss; exposed polyimide requires protective oxide or fluoropolymer coatings.	[121, 125]
VUV	PI	Flexible substrate	VUV can induce chain scission, crosslinking, embrittlement, and optical/ mechanical degradation in polymer substrates.	[126]
Thermal cycling	Glass/polymer substrate stack	Substrate support	Coefficient of thermal expansion (CTE) mismatch between substrate, encapsulant, electrode, and active stack can drive interfacial stress, cracking, or delamination.	[127, 128]

leads to a clear Au signal extending into the perovskite and mesoporous layers. Fig. 12c supports this observation by revealing a laterally uniform Au distribution across the analyzed area. Together, these results show that elevated temperature enables gold to diffuse through spiro-OMeTAD into the absorber, driving irreversible degradation [132].

Another electrode-related degradation pathway has been reported by Svanström et al., who investigated the long-term chemical impact of Cu contacts on iodide perovskites using masked ex situ XRD measurements [133]. As shown in Fig. 12d, regions of PbI_2, FAI, $Cs_{0.17}FA_{0.83}PbI_3$, and $MAPbI_3$ that were not covered by Cu remain structurally stable even after two months of air storage, confirming that ambient exposure alone does not induce bulk degradation. In contrast, Cu-covered regions exhibit a clear time-dependent structural evolution: while PbI_2, $Cs_{0.17}FA_{0.83}PbI_3$, and $MAPbI_3$ show little change within 24 h, the diffraction peaks of FAI nearly vanish over the same period, indicating rapid conversion into an amorphous Cu-FA-I reaction product. After two months, all Cu-covered samples show a pronounced loss of the parent perovskite or PbI_2 reflections, accompanied by the emergence of new diffraction peaks that are absent in the Cu-free regions. These new peaks are assigned partly to CuI, but more notably to the mixed Pb–Cu iodide hydroxide phase siidraite, $[Pb_4(OH)_4][Cu_2I_6]$, demonstrating that Cu contact promotes long-term bulk transformation of the absorber into stable secondary corrosion phases rather than simple surface passivation. Together, the data in Fig. 12d provides compelling evidence that Cu electrodes, under realistic oxygen and humidity exposure, can drive progressive bulk degradation of lead-iodide perovskites, underscoring the necessity of continuous diffusion barriers and robust encapsulation to prevent direct Cu/perovskite contact [133]. Although copper electrodes have been shown to undergo pronounced degradation under terrestrial conditions, dedicated studies that systematically investigate copper-specific electrode degradation under space-relevant environments are still lacking, highlighting an important gap in the current literature.

4.7. Integrated vulnerability map and material-selection metrics

To further support the material-selection discussion, Table 4 summarizes key reliability metrics for materials commonly used or considered in perovskite TSCs, including AO erosion yield, glass-transition temperature (T_g), CTE, and yellowing index (YI). For space-facing layers, AO erosion yield indicates the resistance of the outer barrier, electrode, or encapsulation layer against surface recession and oxidation in LEO [125,146]. T_g is important for polymeric encapsulants and interfacial layers because operation near or above T_g can soften the material, reduce dimensional stability, and increase the risk of creep or interfacial failure during thermal cycling. CTE provides a measure of thermal-expansion mismatch between adjacent layers, which can generate residual stress, cracking, and delamination in multilayer photovoltaic stacks [161]. YI is relevant for transparent substrates and encapsulants because UV/radiation-induced yellowing reduces optical transmittance and can lower photon delivery to the top cell [162]. Therefore, material selection for space-compatible TSCs should be based on the combined balance of AO resistance, chemical durability, thermomechanical compatibility, and optical stability.

Building on the material-selection metrics, Fig. 13 provides an integrated weakness–stressor map for perovskite-based TSCs. The map highlights that the dominant vulnerable region changes with the stressor: radiation mainly affects defect formation and bottom-cell/ interconnect stability, AO and UV primarily challenge exposed

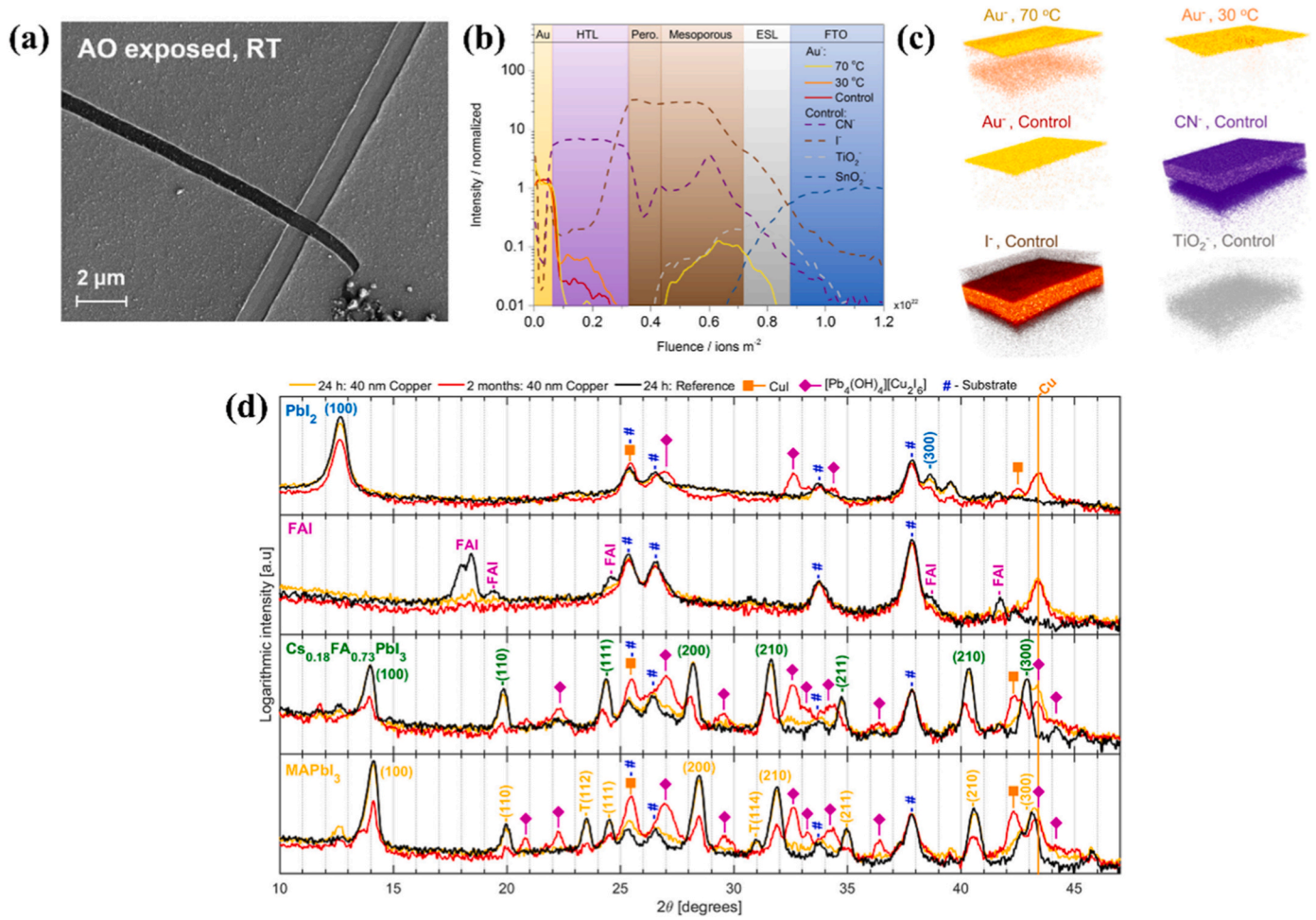

Fig. 12. Materials and device diagnostics relevant to space/operational aging and metal-induced perovskite degradation. (a) High-magnification SEM image of CV-1144-0 after atomic oxygen exposure at room temperature, showing the surface morphology and AO-induced microstructural changes at ×20,000 magnification [131], (b) ToF-SIMS depth profile of an aged PSC, tracking selected ionic species across the control device and comparing the Au^- signal with devices aged at 30 °C and 70 °C. (c) Reconstructed 3D elemental ToF-SIMS maps for the ions traced in (b), acquired over a 10 × 10 μm analysis area [132]. (d) XRD patterns (log-scale intensity) of thin films measured with Cu Kα radiation at θ = 2°, comparing samples with and without Cu; PbI_2 and perovskite reflections are indexed to the cubic phase, with two tetragonal-phase peaks marked "T" [133].

surfaces and optical/transport layers, while thermal cycling and LILT introduce mechanical, transport, and phase-stability limitations.

5. Modeling and experimental correlation

After understanding how space-relevant stressors degrade TSCs in a layer-by-layer manner, simulation-based studies provide an additional route to analyze how these stressors interact with complex multilayer device stacks. Multiphysics modeling is increasingly used to complement experiments by translating radiation exposure, thermal conditions, and material properties into spatially resolved damage metrics and electrical response. In this section, we review the use of Monte Carlo simulations, device-level electrical simulations, density functional theory, and molecular dynamics simulations to study stress-induced effects and identify vulnerable regions within TSC architectures.

5.1. *Physical modeling of radiation transport and device response*

Simulation methods are valuable because they reduce experimental cost and time by predicting degradation trends before a space-relevant test. Simulations help identify vulnerable layers, estimate damage profiles, and guide material or device design before experiments. In this section, the methods are divided into physical modeling and chemical/atomistic simulations. Physical modeling includes Monte Carlo and device-physics simulations, which predict radiation-energy deposition, displacement damage, transport losses, and photovoltaic performance. Chemical/atomistic simulations include density functional theory (DFT) and molecular dynamics (MD), which explain composition-dependent electronic structure, defect stability, lattice response, ion migration, and thermally activated degradation pathways.

5.1.1. *Monte Carlo radiation-transport simulations*

Monte Carlo simulations are used to predict how space radiation interacts with multilayer tandem stacks, including where energy is deposited and where displacement damage is likely to occur. This helps identify radiation-sensitive regions before experimental irradiation studies. Geant4 is presented as a modern Monte Carlo toolkit that enables a unified, physics-based description of radiation–matter interactions, and this capability is extended here to γ-ray irradiation by explicitly resolving photon transport and electromagnetic interaction processes in hybrid halide perovskites. Using Geant4, Novoselov et al. simulated γ-ray exposure at standard calibration energies (0.662, 1.17, and 1.33 MeV) and evaluated the depth-dependent energy deposition within millimeter-scale perovskite absorbers [163]. As shown in Fig. 14a, the deposited energy in $FAPbI_3$ remains nearly uniform across the sample depth for all three γ-ray energies, reflecting the high

Table 4
Material-selection metrics for space-relevant perovskite TSC layers, including AO erosion yield, T_g, CTE, and YI.

Material/Layer	Relevance to TSCs	AO erosion yield ($\times 10^{-24}$ cm^3/atom)	T_g (°C)	CTE ($\times 10^{-6}$/°C)	YI
SiO_2	Protective oxide/encapsulation/Substrate	SiO_2 on Kapton: 0.00103; SiO_x/Kapton: 0.01 [125]	1200 (For Silica glass) [134]	0.5 [134]	0.16-0.26 (Silica glass) 0.12 (Quartz/fused silica) [135]
Soda-lime glass	Substrate	NA	540 [136]	7.67 [137]	−0.06 [135]
Ethylene-vinyl acetate (EVA)	Polymer encapsulant	NA	−16.9 [138]	270-300 [139]	0.602 (glass/polymer geometry) [135]
Al_2O_3	Inorganic encapsulation/barrier oxide	<0.025; Al_2O_3 on Kapton: <0.02 [125]	NA	~8.1 [140]	NA
TiO_2	ETL/oxide barrier	0.0067 [125]	NA	9 [140]	3 → 7 after UV exposure (Epoxy + TiO_2) [141]
SnO_2	ETL/oxide barrier	Negligible (0.3% of Kapton's yield) [142]	NA	11.7 [143]	NA
ITO	Transparent electrode/recombination contact/possible outer conductive barrier	0.002 [125]	NA	5.81 [144]	NA
Al	Electrode/Reflective coating	Al: 0; Al-coated Kapton: 0.01-0.1 [125]	NA	24 [145]	NA
Au	Electrode/contact	0 (appears resistant) [125]	NA	14 [145]	NA
Ag	Electrode/contact	10.5 [125]	NA	18 [145]	NA
FEP/Teflon FEP	Space-facing polymer film/encapsulation film	0.20 [146]	80 [147]	80 [148]	NA
PTFE/Teflon	Fluoropolymer encapsulant	0.142 [146]	123 [149]	93-130 [149]	NA
PVDF/Kynar	Protective polymer	1.29 [146]	−40 [150]	127 [151]	NA
Polyimide/Kapton	Flexible substrate/Space polymer	Kapton H: 3.00, Kapton HN: 2.81 [146]	396 [152]	32 [152]	2.31-3.14 (Colorless PI film) [153]
Polyethylene terephthalate (PET/Mylar)	Flexible substrate/polymer barrier	3.01 [146]	78 [154]	20-25 [154]	1-1.2 (UV-stabilized PET) [155]
Epoxy	Adhesive/Sealant	4.21 [146]	191.7 [156]	40-45 [156]	2 → 4 after UV exposure [141]
Polymethyl methacrylate (PMMA)	Polymer additive/encapsulation-related polymer	5.6 [146]	112.7 [157]	60-70 [157]	0-1 [158]
Parylene	Thin polymer encapsulation	Eroded away [125]	~50 [159]	35 [159]	NA
UV-curable epoxy	Encapsulant	NA	NA	NA	5.6-6.1 [160]

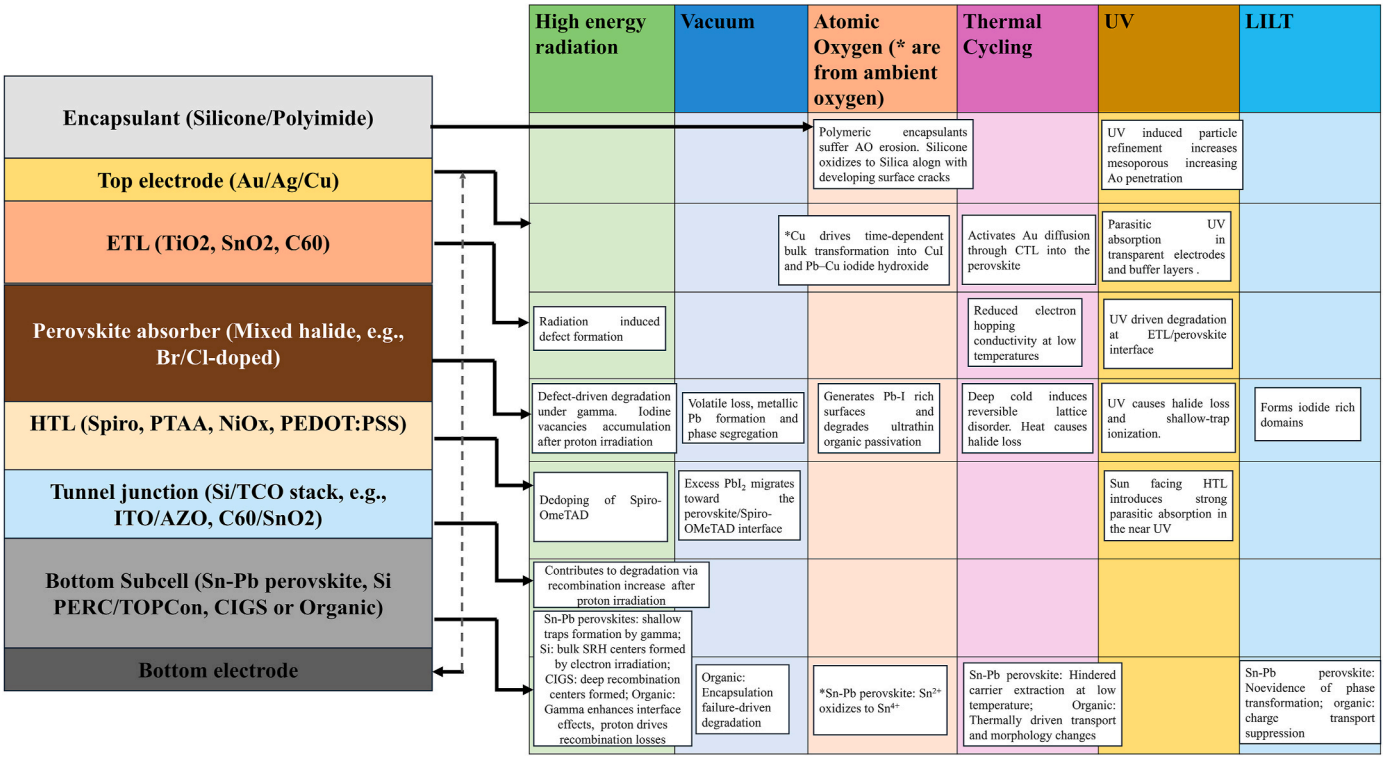

Fig. 13. Weakness-stressor map of perovskite-based TSCs under space-relevant environments. The map identifies the dominant vulnerable layers and degradation pathways associated with high-energy radiation, vacuum, AO, thermal cycling, UV exposure, and LILT operation.

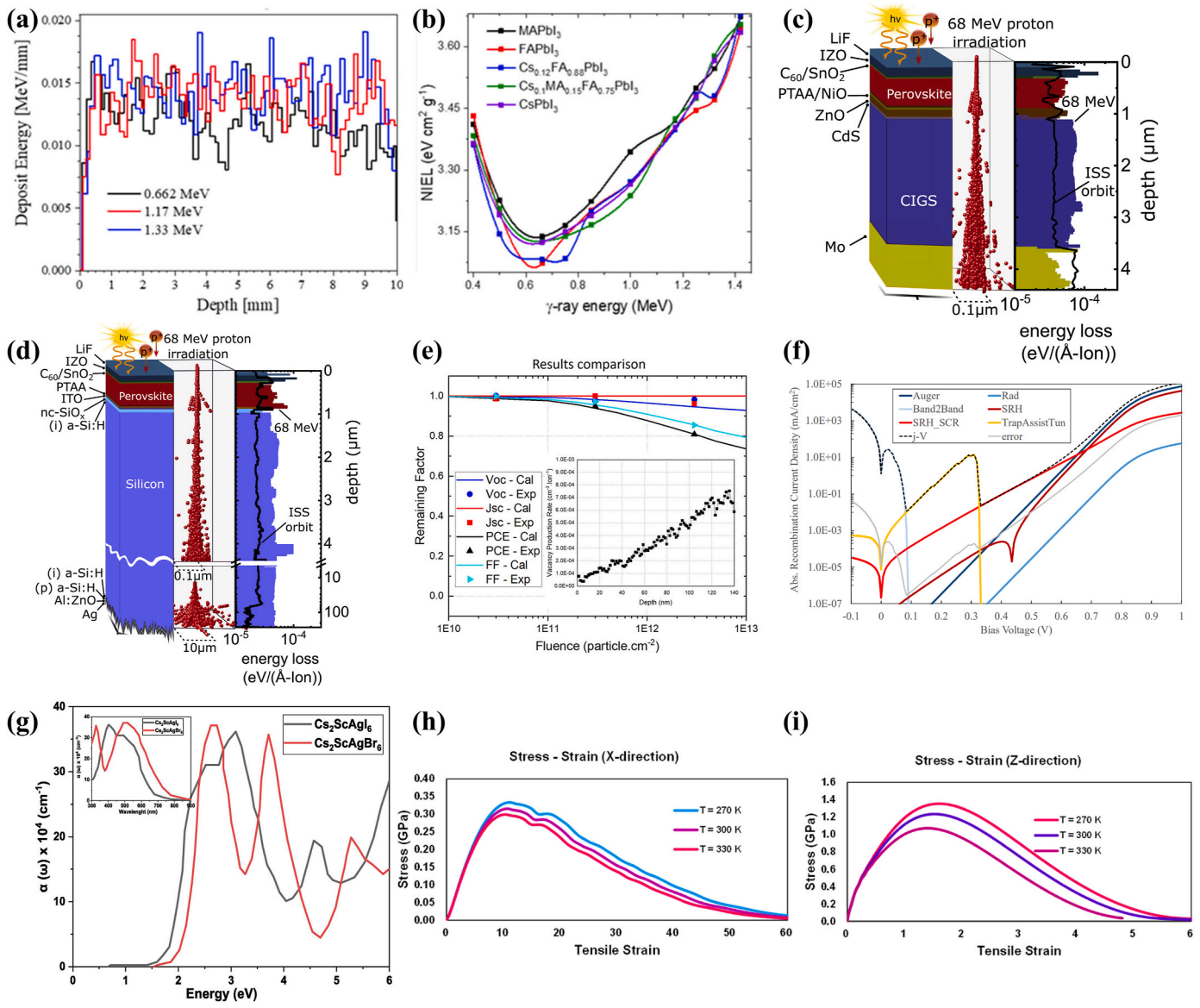

Fig. 14. Multiscale modeling and validation tools for radiation response and TSC performance. (a) Geant4-simulated deposited energy versus perovskite thickness for $FAPbI_3$ at commonly used calibration energies. (b) Geant4-derived NIEL for different halide perovskites [163]; SRIM-based 3D straggling maps for 68 MeV protons in (c) perovskite/CIGS and (d) perovskite/SHJ TSCs, with recoil energy loss plotted versus depth from simulations using 5×10^7 protons; the black line represents an ISS-orbit equivalent damage profile accounting for polyenergetic, omnidirectional proton exposure [62]. (e) Method validation by comparing COMSOL-based calculated results ("Cal") with experimental ("Exp") data reported by Malinkiewicz et al. [164,165] (f) Recombination-current decomposition of the simulated J-V response, comparing the summed mechanism-specific current densities to the total J-V and reporting the residual as an error term [166]. (g) Calculated absorption coefficient of a double perovskite versus photon energy, with the inset showing absorption versus wavelength in the visible range [167]; Molecular-dynamics prediction of temperature-dependent stress in $CH_3NH_3PbI_3$, evaluated along the (h) X and (i) Z directions [168].

penetration depth and low interaction probability of MeV γ-photons. This indicates that γ-ray energy deposition in perovskites is spatially distributed rather than localized, in contrast to the shallow absorption profiles typical of charged-particle irradiation [163].

In addition to electronic energy deposition, Geant4 was used to evaluate the non-ionizing energy loss (NIEL), which reflects displacement-related damage in the lattice. In Fig. 14b, Geant4 simulations show that the non-ionizing energy loss is nearly the same for all investigated perovskite compositions. This reflects the fact that MeV γ-photons primarily deposit energy through electronic interactions, while transferring only a small fraction of their energy to atomic nuclei. As a result, displacement-related damage remains minimal, and variations in chemical composition have little influence on the calculated NIEL values [163]. This work considers millimeter-scale perovskite layers, whereas practical photovoltaic absorbers are typically only a few micrometers thick, limiting direct device relevance. In addition, γ-irradiation studies for perovskite TSCs are largely absent, representing a clear gap in the literature. Similar Geant4 simulations can be extended to tandem architectures and other space-relevant radiation species, including electrons, protons, and heavy ions.

Similar to Geant4, Stopping and Range of Ions in Matter (SRIM) is a Monte Carlo-based simulation tool used to model particle transport and energy loss in matter, particularly for energetic ions. SRIM simulations were employed to calculate the depth-resolved straggling and energy loss of 68 MeV protons in monolithic perovskite/CIGS and perovskite/Si TSCs. As shown in Fig. 14c, the perovskite/CIGS stack exhibits a largely uniform energy-loss profile across the full device thickness, indicating that the proton irradiation probes both sub-cells and interlayers. In

contrast, Fig. 14d shows that in the perovskite/Si TSC, substantial energy loss occurs deep within the silicon bottom cell, consistent with pronounced proton-induced damage in silicon. The simulated profiles closely match the expected damage distribution under International Space Station (ISS) orbital conditions, validating the relevance of the irradiation protocol [62].

5.1.2. Device-physics simulations

Following Monte Carlo radiation-damage modeling, device-physics simulations connect material damage with device-level performance loss. By modeling carrier generation, recombination, extraction, and current matching, these simulations help explain changes in V_{oc}, J_{sc}, FF, and PCE under space-relevant degradation. COMSOL Multiphysics is employed to perform 1D optoelectronic device simulations, incorporating radiation-induced defect profiles into a semiconductor transport model. Nguyen et al. proposed a framework, in which COMSOL Multiphysics is used to implement the optoelectronic device model, where defect distributions calculated from particle simulations are introduced as recombination-active states in the perovskite layer, allowing the simulated current-voltage characteristics to serve as a baseline for assessing radiation-induced performance degradation [164]. Fig. 14e compares simulated and experimental degradation trends to validate the coupled SRIM-COMSOL modeling approach. The calculated remaining factors of V_{oc}, J_{sc}, fill factor, and PCE obtained from the COMSOL device model closely follow the corresponding experimental data reported by Malinkiewicz et al. under proton irradiation [165]. The agreement confirms that incorporating SRIM-derived vacancy profiles as recombination-active defects enables realistic prediction of radiation-induced performance degradation. The inset shows the depth-dependent vacancy production rate used as the defect input for the device simulations [164].

Technology computer-aided design (TCAD) is another widely used framework for device-level electrical simulations of thin-film and TSCs, enabling self-consistent modeling of optical absorption, carrier transport, and recombination under realistic operating conditions. In a numerical study by Alanazi et al., Silvaco Atlas TCAD was employed to analyze a monolithic two-terminal perovskite/Si TSC and to optimize its electrical performance through current matching [169]. The simulated device consisted of a thin-film p-i-n perovskite top sub-cell integrated in series with a thin heterojunction silicon bottom sub-cell via a recombination interface. By systematically varying the absorber thicknesses of the perovskite and silicon layers, the short-circuit current densities of the individual sub-cells were extracted from the TCAD simulations. As shown in Table 5, increasing the perovskite thickness raises the top-cell current while reducing the bottom-cell current, reflecting the optical trade-off inherent to series-connected TSCs. Owing to the 2T architecture, the overall tandem current is constrained by the lower sub-cell current, making current matching a key design requirement. The current matching point was identified as 425 nm, where $J_{sc(top)} = J_{sc(bottom)} = 19.25\ \mathrm{mA/cm^2}$ (with the Si thickness set to 90 μm) [169].

In another work by Boukortt et al., the TSC was simulated because the authors wanted a quantitative device-level estimate of what a two-terminal perovskite/ultrathin-CIGS stack could deliver once both sub-cells are made mutually consistent within a single model [170]. They note that building a suitable TSC model is challenging due to layer-to-layer optical and electrical interactions, so they adopted a stepwise workflow: calibrating the perovskite cell, calibrating the ultrathin-CIGS cell, then simulating the TSC. Since the two sub-cells behave as series diodes, the tandem current is governed by the smaller J_{sc} and the tandem V_{oc} adds, which is why the combined stack must be simulated rather than inferred from isolated cells. Using this approach, they reported a maximum simulated tandem efficiency of 20.84%, with $J_{sc} = 20.56\ mA/cm^2$, $V_{oc} = 1.53V$, and $FF = 66.12\%$ [170].

Along with optimizing the top and bottom absorber sub-cells, the tunnel junction is critical in monolithic TSCs because it must electrically couple the two sub-cells while avoiding additional recombination losses that would degrade the delivered current. Gaspar et al. used TCAD to study a silicon n^+/p^+ tunnel junction in a simplified 1D test structure and then performed a recombination current loss audit of the simulated J-V response [166]. In Fig. 14f, the total recombination current density is decomposed into Auger recombination (Auger), radiative recombination (Rad), Shockley Read Hall recombination (SRH), Shockley Read Hall recombination in the space charge region (SRH_SCR), band to band tunneling (Band2Band), and trap assisted tunneling (TrapAssistTun). Fig. 14f decomposes the simulated tunnel-junction current into the main loss and transport mechanisms and then sums these contributions to reconstruct the simulated J-V curve; the small residual 'error' indicates that the included mechanisms capture the dominant processes governing current flow and recombination in the modeled tunnel junction [166].

5.2. Chemical and atomistic simulations of material stability

5.2.1. DFT simulations

DFT simulations provide materials-level insight into how composition and bonding influence electronic structure, optical absorption, defect formation, and chemical stability. This helps explain why certain absorber compositions or interfaces may be more stable under space stressors. In Fig. 14g, Chargui et al. present the calculated absorption coefficient of the double-perovskite family Cs2ScAgX6 (X = Br, I) as a function of photon energy calculated using the software WIEN2k, with the inset showing the same response across the visible wavelength range [167]. It demonstrates that the proposed top absorber, specifically Cs_2ScAgX_6, exhibits strong visible-light absorption (on the order of $10^5\ \mathrm{cm^{-1}}$), indicating efficient above-bandgap photon harvesting without requiring an excessively thick film. DFT is used here to provide a first-principles screening of optoelectronic and optical properties (absorption strength and related optical response) to justify selecting a double perovskite as the top junction material, and these DFT-derived properties are then carried forward as inputs/constraints for the subsequent tandem modeling and current-matching analysis [167].

In a representative tandem-design workflow, Ravidas et al. first used DFT to quantify the absorber's bandgap and optical response and then ported these outputs into Solar Cell Capacitance Simulator in One Dimension (SCAPS-1D) to simulate a monolithic 2T c-Si/$CsGeI_3$ stack, where current matching determines the final tandem J-V response [171]. Their DFT calculations provided more than a bandgap estimate: $CsGeI_3$ is found to have a direct bandgap of ~1.6 eV, and the density of states (DOS) analysis attributes the band-edge formation largely to Ge and I states, which helps rationalize the use of the lead-free perovskite, which can function as a high-voltage top absorber in a silicon TSC. These DFT outputs are used as SCAPS-1D inputs, enabling the optical filtering of the AM1.5G spectrum through the top stack and a consistent current-matching study against the c-Si bottom cell. In Fig. S5, this integrated workflow shows the current-matched tandem J-V curve, demonstrating the expected series behavior: V_{oc} obtained was ~1.90 V

Table 5
Silvaco Atlas TCAD–simulated short-circuit current density (J_{sc}) of the top perovskite and bottom silicon sub-cells versus perovskite absorber thickness in a monolithic 2T perovskite/Si TSC, illustrating the thickness-driven optical current trade-off and the resulting current-matching point [169].

Top absorber thickness (nm)	Current density (J_{sc}) in $\mathrm{mA/cm^2}$	
	Top cell	Bottom cell
350	18.45	19.86
375	18.76	19.63
400	19.02	19.43
425	19.25	19.25
450	19.44	19.10
475	19.61	18.97
500	19.76	18.85

(approximately the sum of the sub-cells), while J_{sc} was constrained to ~17.55 mA/cm^2, delivering an overall PCE of ~28.43% and thereby connecting first-principles screening directly to the tandem-level performance projection [171]. In summary, DFT provides a material-level basis for selecting tandem top absorbers. SCAPS-1D then converts these inputs into current-matched tandem performance trends.

5.2.2. MD simulations

The previous DFT section motivates composition choice and electronic-level descriptors, but it does not by itself explain atomistic structural evolution, ion migration, lattice distortion, or thermal/mechanical stress tolerance of the perovskite crystal lattice during processing, packaging, or operation. Therefore, MD simulations are needed as complementary approaches to track atomic-scale degradation pathways under space-relevant stressors, including thermal shocks, mechanical loads, and severe temperature variations. Researchers use MD to probe mechanical behavior under operating stressors, since these conditions may alter the lattice structure and atomic arrangement of the perovskite absorber. Henda et al. carried out an MD workflow using the Large-scale Atomic/Molecular Massively Parallel Simulator (LAMMPS), and they presented stress-strain profiles as the key mechanical output [168]. In Fig. 14h, which corresponds to tensile loading along the X direction, the reported ultimate strength, defined as the peak stress reached in the curve, decreases as temperature increases from 270 K to 330 K, dropping from 0.334 GPa at 270 K to 0.315 GPa at 300 K and to 0.299 GPa at 330 K. In Fig. 14i, which corresponds to tensile loading along the Z direction, the same temperature-driven weakening is observed but at higher stress levels, with the ultimate strength decreasing from 1.359 GPa at 270 K to 1.235 GPa at 300 K and to 1.071 GPa at 330 K. Together, Fig. 14h and i shows that increasing temperature reduces the peak stress that the $CH_3NH_3PbI_3$ structure can sustain, and they also show that the predicted peak stress depends strongly on loading direction because the Z direction values remain substantially higher than the X direction values at each temperature. Integrating the mechanical stability of the absorber layer is essential for projecting the long-term durability of TSCs, which must withstand cyclic thermal and mechanical stresses during field operation. MD simulations demonstrate that the mechanical tolerance of the perovskite crystal lattice is both temperature-dependent and highly anisotropic, with the ultimate strength decreasing as operating temperatures rise. Beyond structural screening, MD frameworks allow for the atomic-level simulation of ion migration kinetics across sub-cell interfaces and the prediction of phase stability under severe thermal loads. These insights are critical for designing strain-resistant ICLs and ensuring the structural integrity of the entire tandem stack [168].

6. Mitigation strategies and engineering solutions

Moving from simulation insights, the current section focuses on mitigation strategies used in TSCs and PSCs to improve stability and performance under space-relevant conditions.

6.1. Composition tuning

Among mitigation strategies for perovskite-based TSCs, composition tuning is a direct lever because it can simultaneously set the tandem-relevant bandgap and reduce intrinsic instability pathways. Beal et al. targeted an ~1.8 eV top-cell bandgap needed for Si TSCs and noted that MA-based mixed-halide perovskites can suffer photoinduced halide phase segregation and thermal degradation, which limits stable operation [172]. They therefore replaced MA with inorganic Cs (lower volatility) and tuned the halide ratio in $CsPb(Br_xI_{1-x})_3$, showing a bandgap increase with Br content. Importantly, they identified a stability-composition window: $x \leq 0.4$ avoids strong PL peak shifts under ~1-sun illumination, while $0.2 < x < 0.4$ is highlighted as most attractive because lower x favors the non-perovskite δ-phase and higher x shows illumination-driven segregation; based on this, they selected $CsPbBrI_2$ ($x \sim 0.33$, ~1.9 eV) with improved thermal robustness indicated by comparatively stable absorption behavior at 200 °C versus $MAPbI_3$ [172].

Xu et al. demonstrated that by moving from conventional I/Br WBG alloys (prone to segregation and V_{oc} loss) into a triple-halide (I/Br/Cl) compositional space designed for tandem-relevant bandgaps and improved photostability [173]. Starting from Cs/FA-based WBG hosts, they raised and stabilized the bandgap via controlled Cl alloying (e.g., $MAPbCl_3$ incorporation) and showed that the resulting films remain single-phase over a useble alloy range with measurable Cl incorporation and uniform halide profiles. This compositional strategy is linked to better bulk optoelectronic quality like higher mobility/lifetime, reduced dark carrier density and suppression of illumination-driven segregation, which in turn lowers V_{oc} losses and supports stable semitransparent top cells in high-efficiency two-terminal perovskite/Si TSCs built on the optimized triple-halide top absorber [173].

Another way of composition tuning is to add a stabilizing fourth A-site cation, rather than only adjusting the halide ratio for bandgap. Susic et al. reported that vacuum-deposited CsMAFA mixed-halide WBG films can be thermally fragile: during 85 °C aging, due to the faster formation of PbI_2 and δ-phase signatures, consistent with loss of the perovskite phase [174]. They tried to mitigate this by incorporating GA^+ (quadruple-cation CsMAFAGA) via controlled co-sublimation, which yielded improved structural/phase stability over multi-week stressing [174]. Overall, these studies indicate that tandem reliability can be meaningfully improved by engineering the absorber composition within tandem-compatible bandgaps, using cation and halide choices that suppress segregation and delay heat-driven phase degradation. In practice, this makes composition tuning a foundational mitigation strategy that should be co-optimized with the device stack for long-term stability.

6.2. Radiation-hard and AO-resistant transport/encapsulation layers

Primary studies increasingly indicate that improving the space stability of perovskite (and perovskite TSC) photovoltaics often depends as much on transport layers and encapsulation as on the absorber itself. Rather than relying on a single fix, the literature supports a multi-layer defense against proton-driven damage and AO erosion: (i) CTL hardening, where replacing dopant-dependent organic HTLs with more radiation-robust alternatives (e.g., polymeric HTLs) can reduce ion-migration-linked degradation at high fluence [175], and where inorganic HTLs require stoichiometry control to limit radiation-activated trap formation, including at recombination contacts in TSCs [62]. (ii) AO and low-energy proton shielding, where oxide barrier layers (e.g., micron-scale SiO_x) have been demonstrated to strongly suppress AO attack and can also provide stopping power for low-energy protons before they reach active layers [176]. (iii) Advanced encapsulation for flexible substrates includes ALD-based oxide nanolaminates and silica-forming coatings: ALD coatings have been validated to strongly reduce AO erosion of polymer cover films, while perhydropolysilazane (PHPS)-derived silica layers are reported to form a densified, protective SiO_x surface upon oxidative exposure, supporting improved durability in oxidizing environments [177–179]. However, these protective layers also introduce design costs that must be considered in tandem architectures. Oxide barriers and multilayer encapsulation can increase areal mass, add residual stress, reduce flexibility, introduce parasitic absorption or reflection losses, and modify the optical field entering the top cell. In 2T TSCs, even small changes in front-side transmission or spectral filtering can alter current matching between the sub-cells, so improved environmental shielding may come at the expense of optical and mechanical optimization. Collectively, these layer-specific approaches show a practical pathway to reduce degradation under space-relevant hazards but should be viewed as trade-off-based design strategies rather than universally beneficial additions. For

space-compatible TSCs, the optimal barrier must therefore balance AO/radiation protection with low mass, low optical loss, mechanical compliance, and minimal disturbance to sub-cell current matching.

6.3. Structural and stress engineering for space-environment stressors

As already seen in section 3.2, Jiang et al. report that low pressure under illumination accelerates decomposition/phase changes of the perovskite (initiating at grain boundaries) with outgassing and defect formation [67]. These defects further accelerate migration of species such as Li, Au, I, and Br across the device; they rationalize the vacuum/illumination degradation in terms of two structure-dependent controls: the gas permeability of layers above the perovskite and mobile-ion-induced chemical reactions at charge-transport layers and interfaces. To mitigate these stressors, two engineered stacks are compared to the baseline: a permeability-focused structure B (ITO/SnO2/OHP/Spiro-OMeTAD/Au/Ni/Al) that uses a much thicker Au/Ni/Al top electrode to retard outgassing, and a structure C (ITO/P-TAA/OHP/PCBM/ZnO/AZO/(Ni/Al grid)) intended to minimize both permeability-driven outgassing and ion-accumulation-driven interfacial degradation, with the paper explicitly noting that structure C has been used in TSCs. Under maximum power point (MPP) tracking at 5×10^3 Pa for 1037 h, structure C is reported to reach a PCE loss rate of 0.007%/h (after the initial period) and a projected T80 of 4750 h, making this architecture suitable for the top cell of the TSC which provides a perovskite sub-cell with transport layers and contacts that better tolerate vacuum/space-like operation [67].

Chen et al. frame stress engineering as a structural strategy to mitigate thermal-cycling fatigue in perovskite PV stacks, where residual stresses arise during temperature changes because different layers expand/contract differently, ultimately driving mechanical failure such as cracking and delamination in multilayer devices [180]. They report controlling the residual stress/strain in the perovskite-containing stack by incorporating an alkyl-ammonium additive (notably n-octylammonium iodide (OAI)) so that the perovskite film's residual stress after annealing is reduced, which is associated with suppressed cracking/delamination during thermal cycling. Although this study reports stress engineering in a single junction perovskite solar cell, TSCs are also built as tightly bonded stacks of many thin layers, which can build up stress when the temperature repeatedly goes up and down. So, a stress-engineering approach that keeps the perovskite layer close to no built-in stress and helps the interfaces stay well attached can be used as a practical design method to make tandem stacks more resistant to thermal-cycling damage [180]. More broadly, similar structure and stress engineering logic can be applied to screen and select device stacks that are better matched to specific environmental conditions (e.g., vacuum, thermal cycling, or radiation) by targeting the dominant transport and interfacial failure pathways under each stressor.

6.4. ICL optimization

The optimization of the interconnect region is critical for minimizing voltage losses and ensuring the structural integrity of perovskite TSCs. In perovskite/Si architectures, the replacement of standard sputtered ITO recombination layers with tunable p/n nanocrystalline silicon (nc-Si/nc-SiO_x) junctions has been shown to minimize parasitic absorption and refractive index mismatch. Advanced integration of Tunnel Oxide Passivated Contacts (TOPCon) with highly doped nc-Si ($>2 \times 10^{20}$ cm^{-3}) further enhances radiation tolerance by facilitating efficient Esaki tunneling and passivating the silicon bottom cell against surface recombination [181]. To mitigate sputter-induced damage to the perovskite absorber during top-electrode deposition, solution-processed AZO nanoparticles have been demonstrated to act as an effective buffer layer that also enhances optical absorption through intrinsic roughness. For radiation-hard Perovskite/CIGS TSCs, which notably retain over 85% efficiency after high-energy proton irradiation (68 MeV), original research identifies the primary degradation mechanism not in the absorbers, but as increased non-radiative recombination at the NiO_x HTL [62]. Mitigation strategies for this specific vulnerability include hybridizing ALD NiO_x with self-assembled monolayers (e.g., MeO-PhPACz) to passivate surface defects or utilizing robust inorganic Titanium Silicide (TiSi2) interlayers formed via controlled titanium oxidation [182, 183].

In All-Perovskite TSCs, space-induced changes in the ICL, such as work-function shifts, defect formation, or increased contact resistance, could disturb charge recombination and lead to FF loss or S-shaped J-V behavior. Reported mitigation strategies include compact oxide/metal recombination junctions, such as atomic-layer deposited SnO_2 combined with an ultrathin Au layer, where Au acts as a metallic recombination bridge that promotes efficient hole recombination and suppresses parasitic barrier formation [184]. In addition, the transition to fully inorganic metal-oxide interconnects comprising NiO_x and ITO nanocrystals eliminates the thermal instability associated with organic layers like PEDOT:PSS, maintaining 85% efficiency after 2500 h of thermal cycling at 85 °C [185]. However, under LILT conditions characteristic of deep space missions (e.g., Jovian environments), mixed-halide top cells within the tandem stack exhibit phase segregation that induces severe current mismatch and S-shaped J-V distortions, presenting a thermodynamic challenge distinct from the physical interconnect structure [83]. A critical evidence gap remains regarding the synergistic degradation kinetics of these inorganic interfaces under simultaneous combined stressors, such as concurrent Vacuum-UV irradiation, AO fluence, and thermal cycling.

6.5. Packaging and encapsulation selection for tandem stacks

For tandem stacks, encapsulation acts not only as environmental protection but also as an element that shapes stress evolution and spectral delivery to the top junction. Toniolo et al. packaged perovskite/Si TSC minimodules using thermoplastic polyurethane (TPU) and thermoplastic polyolefin (TPO) in a glass/glass vacuum-lamination approach and benchmarked durability using qualification-style tests that included thermal cycling (−40 to 85 °C). Differences noted between TPU and TPO were in terms of their functional roles in the stack: TPU provided stronger mechanical dissipation across the relevant temperature range, supporting improved tolerance to cycling-induced interfacial damage, whereas TPO maintains higher UV transparency, limiting encapsulant-induced spectral losses that can otherwise shift the top-cell photocurrent and impact current matching [128].

In line with the above study, Bristow et al. reported that the packaging and encapsulation are closely tied to delamination control in monolithic perovskite/Si TSCs, where mechanically weak interfaces can be compromised during module-integration steps such as cell cutting, metallization, and vacuum lamination. In glass-glass packages using a commercial TPO encapsulant with a butyl-rubber edge seal, delamination can be initiated in mechanically stressed samples and then propagate during IEC-style thermal cycling (−40 to 85 °C, 50 cycles). Encapsulant selection, therefore, becomes a practical mitigation lever: delamination is still observed after cycling with a polyolefin elastomer (POE), whereas TPU eliminates delamination after lamination and thermal cycling. A TPU/TPO bilayer is additionally examined to balance delamination resistance with electrical insulation requirements. In this sense, module-integration results reinforce that TPU can prevent delamination that develops with TPO/POE encapsulation during thermal cycling of perovskite/Si TSCs, emphasizing the role of mechanical damping and strain accommodation in the encapsulant layer [186].

Along with the thermal and mechanical packaging, radiation-hard packaging should also be considered. Under high-energy electrons, gamma-ray, and proton irradiation, perovskite absorbers can undergo bulk degradation through the formation of vacancies, interstitials, and trap states, particularly iodine-related defects. These radiation-induced defects can disturb the perovskite lattice, increase non-radiative

recombination, shorten carrier diffusion length and lifetime, and ultimately reduce J_{sc}, V_{oc}, FF, and PCE. Therefore, improving absorber quality alone is insufficient; the packaging design must also reduce the radiation burden reaching the active layers while preserving optical transmission and current matching. Because packaging simultaneously controls radiation exposure, environmental isolation, stress transfer, and spectral delivery, encapsulant selection becomes a central design factor rather than a secondary module-integration step [61,87,187].

Beyond polymer encapsulants, radiation-hard packaging should also consider front-side cover glass and shielding design. NASA studies on solar-cell cover materials show that cerium-doped cover glass improves resistance to electron- and proton-induced optical darkening, while cover glass thickness can attenuate and reshape the proton spectrum before it reaches the active cell layers. Such shielding modifies the displacement-damage profile inside the device and can reduce direct radiation exposure of the absorber and transport layers. For perovskite TSCs, radiation-resistant transparent covers should therefore be co-designed with encapsulant choice, optical transmission, areal mass, mechanical flexibility, and tandem current-matching requirements [188,189].

7. Standardization and qualification perspectives

To interpret vacuum/UV/radiation stability results in a space-testing context, it helps to refer to established space PV and irradiation standards. These standards specify what should be controlled and reported, such as vacuum thermal cycling and UV tests at the assembly level, AM0 calibration rules, and how to run electron/proton irradiation tests, so results from different labs can be compared fairly.

ECSS-E-ST-20-08C (Rev.2, 2023) by European Cooperation for Space Standardization defines space-use requirements for qualifying and procuring photovoltaic assemblies, solar-cell assemblies (SCAs), bare cells, cover glasses, and related diodes, but it is limited to crystalline Si and GaAs cells (>50 μm) and explicitly excludes thin-film technologies. Within its scope, it prescribes space-relevant tests such as vacuum thermal cycling (e.g., 10 cycles at $<2 \times 10^{-3}$ Pa with continuity/insulation monitoring) and UV exposure tests in vacuum (200–400 nm, controlled temperature), with pass/fail criteria such as <2% J_{sc} loss after UV for SCAs. After understanding the qualification style space PV requirements, it is essential to ensure that AM0 performance data are measured and calibrated consistently across laboratories. ISO 15387:2005 standardizes measurement and calibration procedures for single-junction space solar cells, anchoring ratings to an AM0 reference by measuring irradiance with an AM0 standard solar cell tied to a reference extraterrestrial spectral irradiance distribution. It requires AM0 standard cells to be conditioned at one solar constant (1367 W/m^2) for 48 h at 25 °C ± 5 °C, maintain ≤ ±1% spectral mismatch error and ≤1% drift, and be calibrated as I_{sc} per unit irradiance at 25 °C ± 1 °C, using four-wire (Kelvin) connections for accurate electrical measurement.

Another standard by the International Organization for Standardization relevant to space conditions is ISO 23038:2018, because it standardizes electron and proton irradiation test methods for space solar cells, improving comparability across studies. It also justifies common space-testing practice, such as irradiating unshielded (bare) cells, so results remain applicable across different shielding/cover glass designs. The limitation is that the standard does not define data-analysis procedures (it focuses on test conduct), and it does not address other space stressors like thermal cycling, UV, or vacuum outgassing within the same framework. Along with this ECSS-Q-ST-70-06C also outlines procedures for particle (including electron/proton) and UV irradiation testing of spacecraft materials under controlled environmental conditions, with tests performed in vacuum ≤10^{-3} Pa and with defined approaches for setting acceleration factors and monitoring key parameters (e.g., temperature, vacuum, contamination). It also addresses combined exposures (sequential or partly simultaneous) to capture UV–particle synergistic effects more realistically than single-stressor tests. Its limitation for device-performance reviews is that it excludes electronic components, so it does not standardize PV outputs (J-V/PCE) and is mainly applied to materials and interfaces surrounding the solar cell.

Taken together, the above standards provide a solid baseline for single-junction space PV qualification, calibration, and irradiation testing, but dedicated standards for TSCs in space are still not available. Tandems warrant their own qualification framework because they introduce failure modes that are not captured by single-junction logic, particularly (i) current matching constraints (spectral shifts, radiation-induced sub-cell imbalance, and optical filtering through the top stack) and (ii) additional vulnerable interfaces (recombination/tunnel junctions, interlayers, and mechanically coupled stacks that can delaminate or electrically degrade under thermal cycling and irradiation). As a result, applying single-junction standards to tandems risks missing tandem-specific degradation pathways and mis-ranking designs that would behave differently under AM0 spectrum, radiation environments, and thermo-mechanical stresses encountered in orbit.

8. Conclusion

Perovskite tandem solar cells (TSCs) have emerged as highly attractive candidates for next-generation space photovoltaics because of their exceptional power-to-weight ratio and high conversion efficiencies. However, their deployment in space is constrained by the complex interactions between multiple functional layers and the harsh extraterrestrial environment. This review demonstrates that the reliability of two-terminal (2T) perovskite TSCs cannot be evaluated solely from the stability of individual materials or single-junction analogues; instead, it must be understood from a tandem-specific perspective that considers layer coupling, current matching, and buried interface stability.

The analysis reveals that degradation in 2T architectures is highly stressor dependent and architecture specific. Space-related stressors, including radiation, ultraviolet exposure, atomic oxygen, thermal cycling, vacuum, and low-intensity low-temperature (LILT) conditions, affect different layers in distinct ways, while localized failures can propagate throughout the tandem stack owing to the series-connected configuration. Among the various components, wide-bandgap perovskite absorbers, charge transport layers, and particularly the interconnecting layer (ICL) represent critical reliability bottlenecks because their degradation directly influences charge recombination, current matching, and overall device efficiency.

A key outcome of this review is the identification of current matching and ICL stability as fundamental design requirements for reliable 2T perovskite TSCs in space environments. Furthermore, the weakness-stressor relationships summarized herein indicate that no single material or layer universally limits performance; instead, reliability depends on the synergistic optimization of absorber composition, interfaces, transport layers, encapsulation, and mechanical compatibility across the entire device stack.

Despite rapid progress, significant knowledge gaps remain. Most available studies focus on isolated materials or single-junction devices, whereas comprehensive tandem-level investigations under combined space stressors are still scarce. Future research should therefore prioritize long-term tandem testing under realistic AM0 conditions, the development of tandem-specific qualification protocols, and the integration of multiscale modeling with experimental validation. Such efforts will provide a deeper understanding of coupled degradation mechanisms and accelerate the realization of robust, lightweight, and radiation-tolerant perovskite tandem solar cells for future space missions.

9. Future outlook

Dedicated tandem qualification protocols are needed that go beyond

single-junction logic by explicitly tracking current-matching stability, buried interconnect degradation, and delamination risks introduced during module integration. Because tandem weak layers can shift when space stressors interact, validation should emphasize combined-stressor testing (e.g., vacuum-UV, AO, thermal cycling, and irradiation) rather than isolated exposures. Progress will also depend on tighter model-experiment feedback loops, where Monte Carlo damage maps (Geant4/SRIM) guide irradiation design and are then translated into calibrated defect-to-performance links through device simulators (COMSOL/TCAD) validated against measured J-V, EQE, and recombination signatures. Finally, deep-space operation requires LILT-focused design rules that address WBG top-cell phase stability and ensure low-temperature charge transport across interlayers, so that current matching and series operation remain stable under low irradiance and extreme cooling. Looking ahead, there is a clear need to extend LCOE concepts to space-relevant photovoltaic systems, where cost effectiveness is governed not only by efficiency but also by end-of-life power retention under combined stressors, qualification and testing burden, and packaging and shielding mass. Developing mission-specific LCOE or cost-per-delivered-energy frameworks for orbital and deep-space operation will be essential to objectively assess the viability of TSCs beyond terrestrial assumptions.

Declaration of generative AI and AI-assisted technologies in the writing process

During the preparation of this work, the authors used ChatGPT (free version, developed by OpenAI) to improve the readability of the review. The AI tool was not used to analyze data. After using this tool, the authors reviewed and edited the content as needed and take full responsibility for the content of the published article.

CRediT authorship contribution statement

Harini Srikanth Rao: Data curation, Investigation, Methodology, Writing – original draft. **Wei-Hao Chiu:** Methodology, Writing – original draft. **Shih-Hsuan Chen:** Conceptualization, Methodology. **Ming-Chung Wu:** Conceptualization, Writing – review & editing. **Kun-Mu Lee:** Conceptualization, Methodology, Writing – review & editing.

Declaration of competing interest

The authors declare that they have no known competing financial interests or personal relationships that could have appeared to influence the work reported in this paper.

Acknowledgement

The authors thank the support from the National Science and Technology Council, Taiwan (Grant Number: 111-2223-E-182-001-MY4), Chang Gung University, Taoyuan, Taiwan (URRPD2R0011).

Appendix A. Supplementary data

Supplementary data to this article can be found online at https://doi.org/10.1016/j.mtener.2026.102359.

Data availability

No data was used for the research described in the article.

References

[1] M.A.M. Escobar, C. Algora, Joule 9 (11) (2025).
[2] M. Doff-Sotta, et al., Energy Convers. Manag. X 16 (2022) 100325.
[3] V. Subramaniam, et al., Photovoltaics Beyond Silicon: Innovative Materials, Sustainable Processing Technologies, and Novel Device Structures, Elsevier, 2024.
[4] M. Taherbaneh, et al., Energy Convers. Manag. 52 (7) (2011) 2518.
[5] J.A. Carr, et al., Acta Astronaut. 205 (2023) 267.
[6] T. Villela, et al., International Journal of Aerospace Engineering 2019 (1) (2019) 5063145.
[7] A. Poghosyan, A. Golkar, Prog. Aero. Sci. 88 (2017) 59.
[8] M.E. Bush, et al., Acta Astronaut. 235 (2025) 235.
[9] H.S. Rao, et al., Sol. Energy Mater. Sol. Cell. 295 (2026) 114015.
[10] S. Kim, et al., Acta Astronaut. (2025).
[11] S. Kyrimis, et al., Energy Convers. Manag. X (2025) 101395.
[12] B.A. Banks, et al., Materials for Space Applications, 851, 2005, p. 331.
[13] T. Colenbrander, et al., Energy Adv. 2 (2) (2023) 298.
[14] C.A. Wolfe, Using Engineering Cameras on Mars Rovers and Landers to Retrieve Atmospheric Dust Loading, 2016.
[15] 3.0 Power - NASA.
[16] Y. Yu, et al., Curr. Opin. Green Sustainable Chem. 44 (2023) 100870.
[17] M.A. Green, et al., Progress in Photovoltaics, 2025, p. 33. NREL/JA–5900-94273).
[18] A. Richter, et al., IEEE J. Photovoltaics 3 (4) (2013) 1184.
[19] W. Shockley, J. Appl. Phys. 32 (3) (1961) 510.
[20] T. Leijtens, et al., Nat. Energy 3 (10) (2018) 828.
[21] J.P. Mailoa, et al., Appl. Phys. Lett. 106 (12) (2015).
[22] W. Chi, et al., ACS Energy Lett. 8 (3) (2023) 1535.
[23] M.H. Futscher, B. Ehrler, ACS Energy Lett. 1 (4) (2016) 863.
[24] C.H. Henry, J. Appl. Phys. 51 (8) (1980) 4494.
[25] Z. Li, et al., Joule 2 (8) (2018) 1559.
[26] P. Holzhey, et al., Joule 7 (2) (2023) 257.
[27] F. Gao, et al., Materials Futures, 2026.
[28] F.J. Ramos, et al., Sci. Rep. 8 (1) (2018) 16139.
[29] S. Kim, et al., Sci. Rep. 11 (1) (2021) 15524.
[30] Y. Yao, et al., Sol. Energy Mater. Sol. Cell. 259 (2023) 112376.
[31] S.R. Kurtz, et al., J. Appl. Phys. 68 (4) (1990) 1890.
[32] A. Paul, et al., ACS Energy Lett. 9 (6) (2024) 3019.
[33] J. Werner, et al., ACS Energy Lett. 1 (2) (2016) 474.
[34] M.H. Miah, et al., RSC Adv. 14 (23) (2024) 15876.
[35] Z. Qiu, et al., Nano Energy 53 (2018) 798.
[36] H. Shen, et al., Energy Environ. Sci. 11 (2) (2018) 394.
[37] D.N. Micha, R.T. Silvares Junior, Sci. Rep. 9 (1) (2019) 20055.
[38] M. Piralaee, et al., Appl. Opt. 63 (30) (2024) 7940.
[39] J. Chantana, et al., Opt. Mater. 113 (2021) 110819.
[40] S.S. Azad, et al., Sci. Rep. 14 (1) (2024) 6466.
[41] T. Leijtens, et al., Nat. Commun. 4 (1) (2013) 2885.
[42] R.K. Kothandaraman, et al., Small Methods 4 (10) (2020) 2000395.
[43] R. Liu, et al., RSC Adv. 10 (20) (2020) 11551.
[44] D.H. Kim, N.-G. Park, Acc. Mater. Res. 6 (9) (2025) 1147.
[45] H.S. Rao, et al., Chem. Eng. J. (2026) 177494.
[46] G.J. Aalbers, et al., Nat. Commun. 15 (1) (2024) 1276.
[47] Z. Liu, et al., J. Mater. Chem. C 13 (21) (2025) 10891.
[48] Q. Han, et al., Sci. Bull. 64 (19) (2019) 1399.
[49] W. Zhang, et al., Adv. Mater. 37 (8) (2025) 2414125.
[50] H. Bian, et al., J. Mater. Chem. A 11 (1) (2023) 205.
[51] K. Datta, et al., ACS Appl. Energy Mater. 4 (7) (2021) 6650.
[52] M. Saliba, et al., Energy Environ. Sci. 9 (6) (2016) 1989.
[53] D.P. McMeekin, et al., Science 351 (6269) (2016) 151.
[54] M. Saliba, et al., Science 354 (6309) (2016) 206.
[55] Y. Lin, et al., ACS Energy Lett. 2 (7) (2017) 1571.
[56] M.R. Samatov, et al., J. Phys. Chem. Lett. 15 (50) (2024) 12362.
[57] Z. Huang, et al., ACS Energy Lett. 4 (7) (2019) 1521.
[58] G.E. Eperon, et al., Science 354 (6314) (2016) 861.
[59] J. Zhou, et al., Nat. Commun. 15 (1) (2024) 2324.
[60] J. Wu, et al., Angew. Chem. 137 (22) (2025) e202424515.
[61] L. Zhang, et al., Mater. Adv. 6 (22) (2025) 8490.
[62] F. Lang, et al., Joule 4 (5) (2020) 1054.
[63] F. Lang, et al., Adv. Energy Mater. 11 (41) (2021) 2102246.
[64] H.K.H. Lee, et al., Sol. RRL 6 (6) (2022) 2101037.
[65] D.M. Tobnaghi, et al., Int. J. Electrochem. Sci. 9 (6) (2014) 2824.
[66] Ö. Yağci, et al., Radiat. Eff. Defect Solid 172 (11–12) (2017) 805.
[67] Y. Jiang, et al., Joule 4 (5) (2020) 1087.
[68] Y.J. Hofstetter, et al., Front. Chem. 8 (2020) 66.
[69] Y. Wang, et al., Nat. Commun. 14 (1) (2023) 1819.
[70] R. Datt, et al., Appl. Phys. Lett. 126 (25) (2025).
[71] G. Li, et al., Adv. Energy Mater. 12 (48) (2022) 2202887.
[72] R. Guo, et al., Nat. Energy 6 (10) (2021) 977.
[73] S. Ahn, et al., Chem. Eng. J. 496 (2024) 153974.
[74] L. Shi, et al., Science 368 (6497) (2020) eaba2412.
[75] P. Mariani, et al., Nat. Commun. 15 (1) (2024) 4552.
[76] D. Schreurs, et al., J. Mater. Res. 33 (13) (2018) 1841.
[77] T.K. Minton, Protocol for Atomic Oxygen Testing of Materials in Ground-based Facilities, 1995.
[78] B.A. Seid, et al., Small 20 (30) (2024) 2311097.
[79] S.A. Westrick, et al., Atomic oxygen impacts on materials international space station experiment (MISSE)-16 flight samples, in: 2nd International Orbital Debris Conference, 2023.
[80] M. Keshavarz, et al., Adv. Mater. 31 (24) (2019) 1900521.
[81] J. Zheng, et al., ACS Energy Lett. 4 (11) (2019) 2623.

[82] S. Lee, et al., Adv. Funct. Mater. 32 (35) (2022) 2204328.
[83] S. Ozen, et al., Advanced Materials, 2025 e17703.
[84] P. Stella, H. Somberg, Development of Integral Covers on Solar Cells, 1971.
[85] P.-C. Huang, et al., Langmuir 40 (23) (2024) 11873.
[86] Y. Yuan, et al., Nat. Mater. 23 (3) (2024) 391.
[87] H. Huang, et al., ACS Appl. Mater. Interfaces 16 (47) (2024) 65108.
[88] Z. Yu, et al., Nat. Energy 5 (9) (2020) 657.
[89] D. Zhao, et al., Nat. Energy 3 (12) (2018) 1093.
[90] C. Li, et al., Adv. Energy Mater. 8 (36) (2018) 1801954.
[91] Q.-Q. Chu, et al., Matter 5 (9) (2022) 2584.
[92] K. Ungeheuer, et al., Appl. Sci. 15 (2) (2025) 754.
[93] U. Erdil, et al., Energy Technol. 13 (1) (2025) 2401280.
[94] F. Sahli, et al., Adv. Energy Mater. 8 (6) (2018) 1701609.
[95] T. Leijtens, et al., ACS Energy Lett. 2 (9) (2017) 2159.
[96] C. Park, et al., ACS Energy Lett. 5 (10) (2020) 3285.
[97] J. Nespoli, et al., Chem. Mater. 37 (19) (2025) 7611.
[98] Y. Bai, et al., Nat. Commun. 16 (1) (2025) 7344.
[99] B.K. Durant, et al., Sol. Energy Mater. Sol. Cell. 230 (2021) 111232.
[100] D. Meggiolaro, et al., J. Phys. Chem. Lett. 11 (9) (2020) 3546.
[101] J. Xu, et al., ACS Energy Lett. 6 (12) (2021) 4220.
[102] F.-J. Ma, et al., Sol. Energy Mater. Sol. Cell. 274 (2024) 113002.
[103] T.-Y. Lin, et al., J. Mater. Chem. A 12 (13) (2024) 7536.
[104] N. Liu, et al., ACS Appl. Energy Mater. 6 (12) (2023) 6673.
[105] C. Fei, et al., Science 384 (6700) (2024) 1126.
[106] M.B. Islam, et al., ACS Omega 2 (5) (2017) 2291.
[107] A. kumar Anbalagan, et al., RSC Adv. 11 (34) (2021) 20752.
[108] N. Mallik, et al., EES solar 1 (6) (2025) 1004.
[109] G. Wang, et al., Joule 7 (11) (2023) 2583.
[110] J. Zheng, et al., Cell Rep. Phys. Sci. 5 (8) (2024).
[111] Z. Yi, et al., Interdiscip. Mater. 3 (2) (2024) 203.
[112] A. Al-Ashouri, et al., Energy Environ. Sci. 12 (11) (2019) 3356.
[113] A. Al-Ashouri, et al., Science 370 (6522) (2020) 1300.
[114] S. Zhumagali, et al., Adv. Energy Mater. 11 (40) (2021) 2101662.
[115] X.Y. Chin, et al., Science 381 (6653) (2023) 59.
[116] J. Liu, et al., Nature 635 (8039) (2024) 596.
[117] Z. Wang, et al., Polymers 16 (19) (2024) 2845.
[118] R. Sun, et al., ACS Omega 9 (47) (2024) 47324.
[119] B.A. Banks, et al., Consequences of atomic oxygen interaction with silicone and silicone contamination on surfaces in low earth orbit, in: Rough Surface Scattering and Contamination, 3784, SPIE, 1999, p. 62.
[120] A. De Rooij, ESA J. 13 (4) (1989) 363.
[121] B.A. Banks, et al., Atomic oxygen effects on spacecraft materials, in: Ninth International Symposium on Materials in a Space Environment, 2003.
[122] H.C. de Groh III, K.K. de Groh, S.J. Gregor, B.A. Banks, Space exposure of indium tin oxide coatings, NASA/TM–20240002413, NASA Glenn Research Center, Cleveland, OH, 2024.
[123] F. Wang, et al., Gamma irradiation-induced discoloration and annealing characteristics of K9 glass, in: Photonics, 12, MDPI, 2025, p. 538.
[124] G.A. Haynes, Effect of 1 Mev Electrons on ceria-doped Solar Cell Cover Glass, 1973.
[125] B.A. Banks, et al., Atomic oxygen effects on materials, in: NASA, Langley Research Center, NASA (SDIO Space Environmental Effects on Materials Workshop, Part 1, 1989.
[126] H. Shimamura, T. Nakamura, Polym. Degrad. Stabil. 95 (1) (2010) 21.
[127] C. Zhao, et al., Adv. Opt. Mater. 12 (7) (2024) 2301949.
[128] F. Toniolo, et al., Nanoscale 15 (42) (2023) 16984.
[129] P. Gruenbaum, H. Dursch, Space environmental effect on solar cells: LDEF and other flight tests, in: NASA. Langley Research Center, LDEF: 69 Months in Space. Third Post-retrieval Symposium, Part 3, 1995.
[130] D. Chen, et al., J. Photon. Energy 8 (2) (2018) 022601.
[131] D.Z. Chen, et al., ACS Appl. Polym. Mater. 4 (5) (2022) 3627.
[132] K. Domanski, et al., ACS Nano 10 (6) (2016) 6306.
[133] S. Svanström, et al., ACS Mater. Au 2 (3) (2022) 301.
[134] Properties of fused silica. Heraeus Covantics.
[135] D.C. Miller, et al., Examination of an optical transmittance test for photovoltaic encapsulation materials, in: Reliability of Photovoltaic Cells, Modules, Components, and Systems VI, 8825, SPIE, 2013, p. 68.
[136] Y. Wang, et al., J. Alloys Compd. 966 (2023) 171514.
[137] M. Wang, et al., Solid State Sci. 14 (8) (2012) 1233.
[138] R. Polanský, et al., J. Electr. Eng. 64 (6) (2013) 361.
[139] M. Knausz, et al., Polym. Test. 44 (2015) 160.
[140] C.T. Lynch, et al., CRC Handbook of Materials Science, CRC press, Boca Raton, 1974.
[141] A.J. Kadem, et al., Optical Materials, 2025 117550.
[142] K. Gotlib-Vainstein, et al., ACS Appl. Mater. Interfaces 7 (6) (2015) 3539.
[143] P. Peercy, B. Morosin, Phys. Rev. B 7 (6) (1973) 2779.
[144] Tien, C., and Lin, T., coatings (2021).
[145] Thermal Expansion Coefficients at 20 C.
[146] B.A. Banks, et al., Atomic oxygen erosion yield prediction for spacecraft polymers in low earth orbit, in: 11th International Symposium on Materials in a Space Environment (ISMSE), 2009.
[147] K.K. DeGroh, et al., Effects of heating on teflon [R] FEP thermal control material from the hubble space telescope, in: *INTERNATIONAL SAMPE SYMPOSIUM AND EXHIBITION*, SAMPE SOCIETY FOR THE ADVANCEMENT OF MATERIAL, 1999, p. 1014.
[148] FEP: Tetrafluoroethylene/hexafluoropropylene copolymer. NETZSH Proven Excellence.
[149] Y. Araki, J. Appl. Polym. Sci. 9 (2) (1965) 421.
[150] R. Dallaev, et al., Polymers 14 (22) (2022) 4793.
[151] Y. Tai, G. Lubineau, Adv. Sci. 4 (4) (2017) 1600370.
[152] P. Xiao, et al., Polymers 17 (7) (2025) 832.
[153] Y. Shi, et al., RSC Adv. 14 (44) (2024) 32613.
[154] W.A. MacDonald, Large Area and Flexible Electronics, 2015, p. 291.
[155] A. Gok, et al., PLoS One 12 (5) (2017) e0177614.
[156] D. Shen, et al., Sci. Rep. 7 (1) (2017) 2606.
[157] A. Marzocca, et al., Polym. Test. 15 (2) (1996) 179.
[158] H.H. Aung, et al., Integrating Materials and Manufacturing Innovation 12 (4) (2023) 349.
[159] B.J. Coelho, et al., Polymers 15 (10) (2023) 2277.
[160] K. Kowalczyk, A. Kowalczyk, Prog. Org. Coating 89 (2015) 100.
[161] W. Yang, et al., Nano Mater. Sci. (2025).
[162] V. Fiandra, et al., Polym. Degrad. Stabil. 220 (2024) 110643.
[163] I.E. Novoselov, I.S. Zhidkov, Nanomaterials 15 (19) (2025) 1474.
[164] D.-T. Nguyen, et al., Advanced energy and sustainability research 4 (12) (2023) 2300085.
[165] O. Malinkiewicz, et al., Emerg. Mater. 3 (1) (2020) 9.
[166] G. Gaspar, et al., TCAD simulation of electrical characteristics of silicon tunnel junctions for monolithically integrated silicon/perovskite tandem solar cells, in: AIP Conference Proceedings, 2826, AIP Publishing LLC, 2023 070001.
[167] T. Chargui, et al., Sol. Energy 283 (2024) 113016.
[168] M.B. Henda, et al., Eng. Anal. Bound. Elem. 150 (2023) 120.
[169] T.I. Alanazi, et al., Opt. Quant. Electron. 55 (13) (2023) 1152.
[170] N.E.I. Boukortt, et al., Silicon 15 (1) (2023) 293.
[171] B.K. Ravidas, et al., Sol. Energy Mater. Sol. Cell. 267 (2024) 112688.
[172] R.E. Beal, et al., J. Phys. Chem. Lett. 7 (5) (2016) 746.
[173] J. Xu, et al., Science 367 (6482) (2020) 1097.
[174] I. Susic, et al., ACS Energy Lett. 7 (4) (2022) 1355.
[175] S. Tang, et al., Adv. Energy Mater. 13 (25) (2023) 2300506.
[176] A.R. Kirmani, et al., Nat. Energy 8 (2) (2023) 191.
[177] H. Qi, et al., Polymers 14 (2) (2022) 322.
[178] C. Yan, et al., RSC Adv. 14 (47) (2024) 34833.
[179] R. Cooper, et al., Thin Solid Films 516 (12) (2008) 4036.
[180] M. Chen, et al., ACS Energy Lett. 9 (6) (2024) 2582.
[181] B. Marteau, et al., Energies 16 (11) (2023) 4346.
[182] D. Pyun, et al., ACS Appl. Mater. Interfaces 16 (22) (2024) 28379.
[183] F. Guo, et al., Molecules 30 (6) (2025) 1299.
[184] M. Zhang, Z. Lin, Energy Environ. Sci. 15 (8) (2022) 3152.
[185] H. Gao, et al., Sol. RRL 5 (12) (2021) 2100814.
[186] H. Bristow, et al., Sol. RRL 8 (14) (2024) 2400289.
[187] Y. Miyazawa, et al., J. Phys. Chem. C 125 (24) (2021) 13131.
[188] S.R. Messenger, et al., Quantifying low energy proton damage in multijunction solar cells, in: Proceedings of the 19th Space Photovoltaic Research and Technology Conference, 2007.
[189] G.A. Haynes, Effect of Radiation on cerium-doped solar-cell Cover Glass, National Aeronautics and Space Administration, 1970.